

1 **Nucleation and growth of sub-3 nm particles in the polluted urban atmosphere of a megacity in**
2 **China**

3 Huan Yu^{1,2,*}, Luyu Zhou¹, Liang Dai¹, Wenchao Shen¹, Jun Zheng^{1,2}, Yan Ma^{1,2}, Mindong Chen^{1,2}

4 1. School of Environmental Science and Engineering, Nanjing University of Information Science and
5 Technology, Nanjing, China

6 2. Collaborative Innovation Center of Atmospheric Environment and Equipment Technology,
7 Nanjing University of Information Science and Technology, Nanjing, China

8

9 Corresponding authors: hyu@nuist.edu.cn

10

11 **Abstract**

12 Particle size distribution down to 1.4 nm was measured in the urban atmosphere of Nanjing, China in
13 spring, summer and winter during 2014-2015. Sub-3 nm particle event, which is equivalent to
14 nucleation event, occurred on 42 out of total 90 observation days, but new particles could grow to
15 cloud condensation nuclei (CCN)-active sizes on only 9 days. In summer, infrequent nucleation was
16 limited by both unfavorable meteorological conditions (high temperature and RH) and reduced
17 anthropogenic precursor availability due to strict emission control measures during the 2014 Youth
18 Olympic Games in Nanjing. The limiting factors for nucleation in winter and spring were
19 meteorological conditions (radiation, temperature, and RH) and condensation sink, but for the further

20 growth of sub-3 nm particles to CCN-active sizes, anthropogenic precursors again became limiting
21 factors. Nucleation events were strong in the polluted urban atmosphere. Initial $J_{1.4}$ at the onset and
22 peak $J_{1.4}$ at the noontime could be up to $2.1 \times 10^2 \text{ cm}^{-3} \text{ s}^{-1}$ and $2.5 \times 10^3 \text{ cm}^{-3} \text{ s}^{-1}$, respectively, during the
23 8 nucleation events selected from different seasons. Time-dependent $J_{1.4}$ usually showed good linear
24 correlations with a sulfuric acid proxy for every single event ($R^2 = 0.56 - 0.86$, excluding a day with
25 significant nocturnal nucleation), but the correlation among all the 8 events deteriorated ($R^2 = 0.17$)
26 due to temperature or season change. We observed that new particle growth rate did not increase
27 monotonically with particle size, but had a local maximum up to 25 nm h^{-1} between 1-3 nm. The
28 growth rate behavior was interpreted in this study as the solvation effect of organic activating vapor
29 in newly formed inorganic nuclei.

30

31 **1. Introduction**

32 New particle formation (NPF) is an important source of secondary aerosols in the atmosphere
33 (Kulmala et al., 2004a). Field studies and model simulations have consistently shown that NPF can
34 enhance cloud condensation nuclei (CCN) concentrations and contribute significantly to the global
35 CCN production (Wiedensohler et al., 2009; Yue et al., 2011; Spracklen et al., 2008; Pierce and
36 Adams, 2009; Merikanto, 2009; Yu and Luo, 2009; Matsui et al. 2013). NPF is a two-stage process
37 consisting of formation of clusters and subsequent growth to detectable sizes (Kulmala et al., 2000).
38 Recently, chamber experiments have made substantial progress in revealing the fundamental
39 processes involved in particle nucleation and growth (Kirkby et al., 2011; Almeida et al., 2013;
40 Schobesberger et al., 2013; Riccobono et al., 2014; Ehn et al., 2014; Kürten et al., 2014). However,

41 consistent theories are still under investigation to quantify the processes physically, chemically, and
42 dynamically (Kulmala et al., 2013, 2014). For example, the identity and physico-chemical properties
43 of assisting vapors other than sulfuric acid (H_2SO_4) are uncertain so far. It is also uncertain what
44 mechanisms allow the assisting vapors to overcome strong Kelvin effect over sub-3 nm particles.
45 Existing mechanisms include condensation of extremely low volatility organic compounds (Ehn et
46 al., 2014), nano-Köhler activation (Kulmala et al., 2004b), heterogeneous chemical reactions (Zhang
47 and Wexler, 2002), heterogeneous nucleation (Wang et al., 2013), and adsorption of organics on
48 cluster surface (Wang and Wexler, 2013). However, the relative importance of various mechanisms
49 is unknown.

50 Direct measurements of size- and time dependent nucleation rate and growth rate in sub-3 nm
51 size range are important to constrain the relative contributions from different mechanisms and
52 precursors. Such measurements are also important to evaluate the survival probability of new particle
53 to CCN-active sizes (~ 100 nm for soluble particles at 0.2% super saturation, Pierce and Adams, 2009)
54 and to reveal the limiting factors in the process. Recently, a series of new instruments have been
55 developed to measure sub-3 nm aerosol number concentration and chemical composition, such as
56 condensation particle counters (e.g., PSM, DEG-SMPS, Jiang et al., 2011a; Sipila et al., 2009;
57 Vanhanen et al., 2011), ion spectrometers (e.g., NAIS, Asmi et al., 2009), and mass spectrometers
58 (e.g., Cluster-CIMS, APi-TOF, CI-APi-TOF, Jokinen et al., 2012; Junninen et al., 2010; Zhao et al.,
59 2010). Kuang et al. (2012) developed a de-coupling method to measure size- and time dependent
60 growth rates of sub-5 nm particles. Their results at two urban sites in U.S.A showed that
61 size-resolved growth rates increased approximately linearly with particle size from 1 to 5 nm.

62 Similar results were also observed in the Boreal forest (Kulmala et al., 2013; Lehtipalo et al., 2014).
63 Based on growth rates measured below 2 nm, Kulmala et al. (2013) identified three separate size
64 regimes, which were dominated by different key gas to particle conversion processes.

65 The relative contribution of different precursors and mechanisms to the nucleation and growth of
66 1-3 nm particles may vary greatly with atmospheric conditions (Riipinen et al., 2012). Therefore,
67 sub-3 nm particle measurements in a variety of atmospheric conditions, e.g., remote or urban
68 atmosphere, biogenic- or anthropogenic emission dominated areas, are immensely valuable.
69 Unfortunately, such data are very sparse until now (Jiang et al., 2011b; Kuang et al., 2012; Kulmala
70 et al., 2013; Lehtipalo et al., 2009, 2010, 2011; Yu et al., 2014a, b). China is suffering from severe
71 atmospheric particulate matter pollution in recent years (Chan and Yao, 2008; Yue et al., 2011). To
72 the best of our knowledge, only two studies were conducted in China to measure the occurrence of
73 new particles down to ~1 nm. In these two studies, air ions (Herrmann et al., 2014) or neutral
74 particles (Xiao et al., 2015) were measured by AIS or PSM in two urban locations of Yangtze River
75 Delta region. Both studies were conducted in the winter season.

76 Here we reported the nucleation and growth of sub-3 nm particles in the urban atmosphere of
77 Nanjing, China on arbitrarily selected observation days in spring, summer and winter of 2014-2015.
78 Our aim was to (1) provide new information about the initial steps of NPF based on size- and time
79 resolved nucleation rate and growth rate measurements, and (2) find possible limiting factors behind
80 the seasonal and diurnal variations of nucleation events in the polluted urban atmosphere.

81 **2. Methodology**

82 **2.1 Field measurements**

83 Nanjing is the second largest megacity after Shanghai in the Yangtze River Delta (YRD) region
84 of China (Chan and Yao, 2008). The YRD city cluster, covering $2.1 \times 10^5 \text{ km}^2$ land with 170 million
85 residents, is one of the most populated and industrialized regions in China. Field measurement was
86 conducted from the third floor (15m above the ground level) of an academic building beside a
87 Chinese national meteorology observatory facility in NUIST campus (32.20° N , 118.71° E , symbol
88 ① in Figure 1). The sampling was carried out during the months of May (May 10-30, 2014), June
89 (June 1-15, 2014), December (December 24-31, 2014), February (February 16-22, 2015), and March
90 (March 1-7, 2015). Total 58 measurement days were arbitrarily selected to represent spring, early
91 summer and winter seasons, but to avoid any rain-event.

92 As part of an intensive summer campaign (12 August-12 September 2014), the summer
93 measurement was conducted at a local governmental meteorology observatory platform (32.06° N ,
94 118.70° E) that is 14km south to the NUIST site (② in Figure 1). The instruments were housed in an
95 air conditioned trailer, using exactly the same sampling inlets as the NUIST site. The main aim of the
96 summer campaign was to understand the effects of regional emission control measures during the
97 2014 Young Olympic Games (August 1-September 15) on air quality. Because the two sites locate
98 within the same urban air shed, the measurement provided an opportunity to study seasonal variation
99 of nucleation and its relationship with meteorological variables and gaseous precursors.

100 Sub-3 nm clusters/particles (hereafter referred as particles) were measured with a nano
101 condensation nucleus counter system (nCNC) consisting of a Particle Size Magnifier (PSM model
102 A10, Airmodus Oy, Finland) and a butanol Condensation Particle Counter (model A20, Airmodus
103 Oy, Finland). During the measurement, an ambient air flow of 14 standard liters per minute (slpm)

104 was drawn into building room or trailer via a 72 cm long and 1.0 cm I.D diameter stainless steel (SS)
105 tube, which was extended outside the room/trailer horizontally. PSM then sampled a split flow of 2.5
106 slpm via a SS T-union. The design of the inlet tubing (length and air flow rate) was to minimize the
107 transport loss of nano particles. The size dependent transport survival ratios of sub-3 nm particles in
108 the inlet tubing was estimated (67 %-86 % for 1.4-3.0 nm) and corrected using a particle loss
109 calculator tool (von der Weiden et al., 2009).

110 PSM was operated in a continuous scanning mode with a cycle of 240 steps between saturator
111 flow rates of 0.1 and 1.0 slpm within 240 seconds. The particle cut-off sizes of the nCNC varied with
112 saturation ratios in the saturator (Vanhanen et al., 2011). A step-wise method was used to invert raw
113 scanning data to size spectrum (time resolution: 4 minutes) of sub-3 nm particles, which were
114 classified evenly into 6 size bins, i.e. 1.4-1.6, 1.6-1.9, 1.9-2.2, 2.2-2.4, 2.4-2.7, and 2.7-3.0 nm. The
115 inverted particle number concentrations in the 6 bins were referred as $N_{1.5}$, $N_{1.8}$, $N_{2.0}$, $N_{2.3}$, $N_{2.6}$ and
116 $N_{2.8}$, using mean values of upper and lower size boundaries in each bin. The step-wise method was
117 described in detail by Lehtipalo et al. (2014).

118 Particle size distributions in the range from 3 - 750 nm were obtained by integrating two
119 scanning mobility particle spectrometers (SMPS) with a nano-SMPS (a TSI differential mobility
120 analyzer DMA3085 and a condensation particle counter CPC3776; scanning range: 3 - 64 nm) and a
121 long-SMPS (TSI DMA3081 and CPC3775; scanning range: 64 - 750 nm). During the summer
122 campaign, only the long-SMPS was operated to scan particles from 8 - 350 nm. Scanning cycles of
123 both SMPS systems were 4 minutes, in order to synchronize with the nCNC. The SMPSs sampled
124 ambient air from a separate sampling inlet. The inlet was a 129 cm long and 1.0 cm I.D

125 horizontally-oriented SS tube with an air flow of 14 slpm. The transport loss of particles in the SMPS
126 inlets was corrected using size dependent survival ratios of 85-100% for particles > 3 nm.

127 Sulfur dioxide (SO₂), ozone (O₃), carbon monoxide (CO) and nitrogen oxides (NO and NO₂)
128 concentrations were measured every 1 minute with Thermo Environmental Instruments (model
129 43i-TLE, 49i, 48i, and 42i, respectively). When gaseous SO₂, O₃, NO₂ and CO data were not
130 available, hourly SO₂, O₃, NO₂ and CO were obtained from nearby local Environmental Protection
131 Agency (EPA) monitoring station. PM_{2.5} was monitored with Thermo Scientific TEOM 1405.
132 Meteorological variables including wind speed, wind direction, relative humidity (RH), temperature
133 and solar radiation flux were recorded every 1 hour during the measurement periods. Mean
134 concentrations of PM_{2.5}, SO₂, and O₃ were 79 μg m⁻³, 10 ppbv and 48 ppbv, respective, during the
135 whole measurement period. Therefore, we regard our measurement environment as a polluted urban
136 atmosphere.

137

138 **2.2 Nucleation event and growth patterns**

139 A criterion was set to determine whether the nCNC detected sub-3nm particles in the atmosphere.
140 The criterion was that total particle concentration reading followed the supersaturation scanning
141 cycle of PSM so that the highest concentrations were measured at lowest cut-off sizes (see also
142 Figure 2 in Lehtipalo et al., 2014). However, it was possible in the step-wise inversion method that
143 the number concentration fluctuation of > 3 nm particles within a 4-min scanning cycle was wrongly
144 inverted to sub-3 nm particles even when sub-3 nm particles actually did not exist according to the
145 above criterion. As a result, the step-wise inversion method always reported a background sub-3 nm

146 particle concentration (N_{sub-3} , i.e. the sum of $N_{1.5}$, $N_{1.8}$, $N_{2.0}$, $N_{2.3}$, $N_{2.6}$ and $N_{2.8}$) of $0.5 \times 10^3 - 2 \times 10^3$
147 cm^{-3} in the nighttime and $3 \times 10^3 - 8 \times 10^3 \text{ cm}^{-3}$ in the daytime. Similar background levels of sub-3 nm
148 particles during non-NPF periods were also reported by other studies that used the nCNC (Kulmala
149 et al., 2013; Lehtipalo et al., 2014; Xiao et al., 2015). Following their procedures, we did not attempt
150 to subtract this background from N_{sub-3} reported in this study.

151 We defined sub-3 nm particle event as sub-3 nm particle occurrence with N_{sub-3} higher than
152 background level persisting for longer than 1 h in the atmosphere. In this study, we used sub-3 nm
153 particle event as an approximate measure of nucleation event. This is because (1) there was an
154 approximately positive linear correlation between N_{sub-3} and nucleation rate ($J_{1.4}$ in this study, see
155 next section) with R^2 of 0.94 (Figure 2), and (2) N_{sub-3} calculation needs only nCNC scanning data
156 and was thus more readily available than $J_{1.4}$ calculation which needs both nCNC and SMPS
157 scanning data. Similar definition has been discussed in our previous studies (Yu et al., 2014a, b).
158 Apparently, a sub-3 nm particle event did not necessarily lead to an NPF event always, but it
159 indicated the intensity and frequency of nucleation in the atmosphere. One focus in this work was to
160 investigate the characteristics of sub-3 nm particle event.

161 Particle growth after nucleation is crucial to determine if nucleated particles could grow to
162 CCN-active sizes. We identified two growth patterns according to size spectrum characteristics in
163 sub-3 nm size range (Figure 3). In a Type A event (Figure 3a or b), size distribution $n(D_p, t)$ was
164 higher at smaller sizes (e.g., 1.4–1.6 nm) than $n(D_p, t)$ at larger sizes (e.g., 2.7–3.0 nm). The size
165 spectrum below 3 nm thus looked like a “volcano”. In a Type B event (Figure 3c or d), $n(D_p, t)$ was
166 lower at smaller sizes than $n(D_p, t)$ at larger sizes (“up-side-down volcano”). For the size range > 3

167 nm, depending on whether a banana-shape growth was seen, we further defined Type A1/A2 and
168 Type B1/B2 events: particles eventually grew to CCN-active sizes in Type A1 and B1 events, while
169 in Type A2 and B2 events banana-shape particle growth to CCN-active sizes was not seen. Therefore,
170 Type A1 and B1 events were equivalent to conventional NPF events based on either DMPS or SMPS
171 measurements.

172 Type B size distribution was more unusual since $n(D_p, t)$ of small particles were less than $n(D_p, t)$
173 of large particles in the sub-3 nm size range. We excluded the possibility of deteriorated nCNC
174 detection efficiencies for small particles due to high particle loading in the sample air. This is
175 because total number concentrations of nCNC during our measurements never approached nCNC
176 upper concentration limit $4 \times 10^5 \text{ cm}^{-3}$, especially in the early stage of nucleation when total particle
177 concentration was rather low. Our nCNC was also calibrated periodically using $\text{H}_2\text{SO}_4\text{-H}_2\text{O}$ particles
178 in a laboratory flow tube to ensure the detection efficiency of the nCNC. The different chemical
179 composition of atmospheric particles could be another factor of lower detection efficiencies. It is
180 well known that organic substances activate less readily in diethylene glycol (e.g. Kangasluoma et al.
181 2014). However, it is accepted in general that larger particles have higher mass fraction of organics
182 than smaller particles in a NPF process. If organic substances activate less readily in DEG, it should
183 be even more difficult to activate larger particles than smaller particles. Therefore, the increasing
184 $n(D_p)$ with D_p (i.e. upside down volcano) could not be simply due to lower detection efficiency of
185 organic substances.

186 **2.3 Formation rate and growth rate calculations with a simplified GDE method**

187 Conventional appearance time method determined growth rates (hereafter, GR) during the initial
188 period of NPF by finding the time steps when newly-formed particles appeared at certain size bins
189 and calculating the GR from the time differences between successive size bins (Kulmala et al., 2012;
190 Lehtipalo et al., 2014). This method was often not applicable to the NPF event with high GR below 3
191 nm, e.g., 0.3 nm/4 min (i.e. 4.5 nm h⁻¹) with size intervals 0.3 nm and scanning time intervals 4
192 minutes in our measurements. Furthermore, sub-3 nm particles were often generated persistently
193 throughout the daytime period. Maximum concentrations in the sub-3 nm size bins could appear
194 around noontime, which is a few hours later than the onset of nucleation. Therefore, we were not
195 able to pinpoint correctly maximum or 50% maximum concentrations at the onset of nucleation.

196 The rapid growth of small particles in the urban atmosphere was the motivation that we used an
197 alternative method to calculate growth rate and formation rate. Here, we analyzed 8 events (listed in
198 Table 1, including both Type A1/A2 and B1/B2 events) in detail, for which complete size spectra
199 from 1.4 - 750 nm were available without distorted, broken or noisy data. Total 8 size bins were
200 classified: 6 evenly-divided size bins in sub-3 nm and 2 size bins in 3-30 nm (3-10 and 10-30 nm).
201 For an aerosol population that is growing through simultaneous condensation and coagulation,
202 aerosol general dynamic equation (GDE) describes the evolution of number concentration in a size
203 bin between particle diameters D_{p1} and D_{p2} ($D_{p2} > D_{p1}$) as:

$$204 \frac{dN(D_{p1}, D_{p2}, t)}{dt} = J(D_{p1}, t) - J(D_{p2}, t) - \text{CoagSnk}(D_{p1}, D_{p2}, t) + \text{CoagSrc}(D_{p1}, D_{p2}, t) \quad (1)$$

205

206 where $N(D_{p1}, D_{p2}, t)$ is the number concentration from D_{p1} to D_{p2} , inverted from nCNC or SMPS
 207 scanning data. J is condensational growth flux (i.e. particle formation rate) across the lower ($D_{p,1}$) or
 208 upper ($D_{p,2}$) boundaries of a size bin. In the first size bin of 1.4-1.6 nm, $J(1.4 \text{ nm}, t)$, or simply $J_{1.4}$,
 209 is the unknown formation rate of the smallest particles that we measured.

210 $\text{CoagSnk}(D_{p1}, D_{p2}, t)$ and $\text{CoagSrc}(D_{p1}, D_{p2}, t)$ are the sink and source terms defining the
 211 coagulation out of and into the size bin between D_{p1} and D_{p2} . Assuming bin k has lower boundary
 212 $D_{p,1}$ and upper boundary $D_{p,2}$,

$$213 \quad \text{CoagSnk}(D_{p1}, D_{p2}, t) = N(k, t) \sum_{i=1}^{98} (1 - \theta_{k,i,k}) K_{k,i} N(i, t) \quad (2)$$

$$214 \quad \text{CoagSrc}(D_{p1}, D_{p2}, t) = \frac{1}{2} \sum_{i=1}^{k-1} \sum_{j=1}^{k-1} \theta_{i,j,k} K_{i,j} N(j, t) N(i, t) \quad (3)$$

215 Here $N(i, t)$ is number concentration of bin i . $K_{i,j}$ is coagulation kernel for a collision between
 216 particles from bins i and j . Probability coefficient $\theta_{i,j,k} = 1$, if the volume sum of two coagulating
 217 particles ($v_i + v_j$, here the volume is calculated from the center diameter of a bin) is within the
 218 volume boundaries of bin k . otherwise $\theta_{i,j,k} = 0$. The particle coagulation of total 98 bins was
 219 considered, but the coagulation terms were only needed to be calculated for the smallest 8 bins from
 220 1.4 to 30 nm. According to our calculation, $\text{CoagSrc}(D_{p1}, D_{p2}, t)$ accounted for only 0 - 0.8 % of the
 221 total particle flux into a bin (i.e. $\text{CoagSrc}(D_{p1}, D_{p2}, t) + J(D_{p1}, t)$) in the sub-3 nm size range. This
 222 implied that self coagulation played a negligible role and most of the production flux into a bin is due
 223 to condensational growth from gas molecules.

224 The GDE here is the same as the Eq. 1 by Kuang et al. (2012). In their method, gaseous H_2SO_4
 225 was measured simultaneously and a constant $GR(D_p, t) / GR_{\text{H}_2\text{SO}_4}(D_p, t)$ ratio at a given size over time

226 was assumed. Their $GR(D_p, t)$ was then solved by fitting the GDE to the measured size distributions.
 227 In our study, however, we did not measure gaseous H_2SO_4 . Instead, $J(30 \text{ nm}, t)$ in the largest size
 228 bin, which is the condensational growth flux out of 30 nm, was set to zero. This simplification was
 229 valid in the four Type A2/B2 events when particles never grew to $> 30 \text{ nm}$ (March 4, February 19,
 230 May 20 and May 16). In the rest four Type A1/B1 events (February 18, December 27, May 15, and
 231 August 15), this was also valid during the early NPF period when particles did not grow out of 30 nm
 232 and during the late NPF period when particles grew out of 30 nm completely. During the middle
 233 period of events (usually around 11:00 AM-14:00 PM), $J(30 \text{ nm}, t)$ was underestimated and thus
 234 $J_{1.4}$ could be regarded as a lower estimate. In the four Type A2/B2 events, our calculation showed
 235 that J_{10} was only 0-4% of $J_{1.4}$. Xiao et al. (2015) and Kulmala et al. (2013) measured both $J_{1.5}$ and J_3
 236 using appearance time method. Their J_3 was less than 7% of $J_{1.5}$. Furthermore, $J_{30}/J_{1.4}$ ratio should be
 237 even smaller than $J_{10}/J_{1.4}$ or $J_3/J_{1.5}$ ratios, considering the 8 events were carefully selected to ensure
 238 all sub-30 nm particles were grown from nucleation (not emitted directly from emission sources like
 239 vehicular engine). All these evidences supported that even if J_{30} was set to 0, $J_{1.4}$ would not be
 240 underestimated more than 7% when particles grew cross 30 nm on February 18, December 27, May
 241 15, and August 15.

242 Equation 1 requires the balance of condensational growth (J), coagulation terms (CoagSnk and
 243 CoagSrc) and the changing rate of particle number concentration (dN/dt). Using Eq. (1) we can
 244 therefore calculate the nucleation rate $J(1.4 \text{ nm}, t)$ and formation rates $J(D_p, t)$ across all size bin
 245 boundaries from 1.6 to 10 nm. After the formation rates $J(D_p, t)$ were obtained, $GR(D_p, t)$ was
 246 calculated from $J(D_p, t)/n(D_p, t)$, where $n(D_p, t)$ is size distribution calculated as $n(D_p, t) = \frac{dN(t)}{dD_p}$

247 for each size bin. On the other hand, the appearance time method could still be applied to (1) the size
248 range of > 3 nm where size intervals were large (2-6 nm), and (2) the size range of < 3 nm when GR
249 was small. The results from appearance time method will also be showed in the next section.

250

251 **3. Results and discussion**

252 Section 3.1, sections 3.2-3.4 and section 3.5 were organized, respectively, to address the
253 following 3 issues: (1) seasonal variation, diurnal variation and limiting factors of nucleation event
254 (represented by sub-3 nm particle event) in the polluted urban atmosphere, (2) time- and size
255 dependent nucleation rate and growth rate of sub-3 nm particles, and their implications for nucleation
256 and growth mechanisms, (3) Inhibited particle growth to CCN-active sizes in strong nucleation
257 events of Type B2.

258 **3.1 Seasonal and diurnal variations of nucleation event**

259 As seen from Figure 2, there was an approximate linear correlation between N_{sub-3} and $J_{1.4}$ with
260 the slope of $N_{sub-3}/J_{1.4}$ equal to ~ 160 . This seemed to suggest that the average residence time of
261 new particles in the sub-3 nm size range was 160 seconds before they were scavenged due to
262 coagulation or grew out of 3 nm. The sub-3 nm particles observed at the present work were thus
263 formed in situ in the urban atmosphere and not likely to be carried-over by air transport. In this
264 section we used sub-3 nm particle event as an approximate measure of nucleation.

265 We observed significant seasonal characteristics of nucleation event (Figure 4). Nucleation was
266 rare and weak in summer, while it was commonly observed in all other seasons. During our

267 measurements from 2014 to 2015, nucleation events occurred on 81% of all spring observation days
268 (May 2014), 53% in early summer (June 2014), 10% in summer (August and September 2014), and
269 64% in winter (December 2014, February and March 2015). We compared intensity (N_{sub-3}) and
270 frequency of nucleation events, as well as meteorological variables (temperature, RH, wind speed,
271 and solar radiation flux) and gaseous pollutants (SO_2 , NO_2 , CO and O_3) for spring, summer and
272 winter seasons. June was not shown in Figure 4 for comparison, because it was a transit season from
273 spring (May) to summer (August and September). The data were first averaged over the entire event
274 period for each event; and we then used event-averaged data to create box and whistler plots for the 3
275 seasons. $PM_{2.5}$ was used here as a surrogate of condensational sink (CS), because of the more ready
276 availability of $PM_{2.5}$ data than SMPS data.

277 As shown in Figure 4, nucleation in summer was characterized by lowest frequency, lowest
278 N_{sub-3} ($2.2 \times 10^4 \text{ cm}^{-3}$), and short nucleation period (only 1-2 hours). Strict emission control measures
279 during the 2014 Youth Olympic Games resulted in relatively low $PM_{2.5}$ level ($32 \pm 8 \mu \text{ g m}^{-3}$),
280 which should favor nucleation. However, relatively low SO_2 concentration ($1.4 \pm 0.6 \text{ ppbv}$), high
281 temperature ($26 \pm 2 \text{ }^\circ\text{C}$), and high RH ($74.3 \pm 4.2 \%$) might not be in favor of nucleation. A simple
282 H_2SO_4 proxy ($\text{Radiation} \times SO_2 / PM_{2.5}$) indicated that summer H_2SO_4 concentration was likely to be the
283 lowest among the 3 seasons, which could explain low nucleation intensity/frequency.

284 We further examined diurnal variations of N_{sub-3} and other variables on event and non-event days
285 in winter (Figure 5). Because nucleation in winter was characterized by Type B event
286 (“up-side-down volcano” below 3 nm), event days were further divided to Type B1 and Type B2
287 events depending on whether banana-shape particle growth was seen. The difference between Type

288 B1 and B2 will be discussed later in Section 3.5. During the non-event days, N_{sub-3} ranged from
289 $2.4 \times 10^3 \text{ cm}^{-3}$ in the night to 8.0×10^3 in the day, which was close to background levels. During the
290 event days, N_{sub-3} in the night was close to that of non-event days, but could reach $8 \times 10^4 - 20 \times 10^4$
291 cm^{-3} in the middle of the day. This was more than 10 times higher than those on the non-event days.
292 From Figure 5 we can see that non-event day had higher concentrations of anthropogenic precursors
293 (indicated by SO_2 , NO_2 , and CO), but nucleation seemed to be limited by higher pre-existing particle
294 surface area (indicated by $\text{PM}_{2.5}$), higher temperature and RH, and lower radiation flux.
295 Photochemistry indicators O_3 was also lower during non-event days.

296 Nucleation in spring was characterized by highest frequency (81%) among all seasons. Highest
297 gaseous pollutant concentration of (H_2SO_4 proxy, SO_2 , NO_2 , CO and O_3) and radiation seemed to the
298 favorable factors to explain this. However, N_{sub-3} in spring ($3.3 \times 10^4 \text{ cm}^{-3}$) was much lower than that
299 in winter ($11.2 \times 10^4 \text{ cm}^{-3}$). Unfavorable factors included high pre-existing particle surface area ($\text{PM}_{2.5}$:
300 $112 \pm 68 \mu \text{g m}^{-3}$) and high temperature ($27 \pm 4 \text{ }^\circ\text{C}$) in spring. Integrating the above seasonal and
301 diurnal variation information in Figure 4 and Figure 5, we tentatively identified that the limiting
302 factors for nucleation in our urban atmosphere were (1) radiation, temperature, RH and CS in winter
303 and spring, and (2) temperature, RH and available gaseous precursors in summer.

304 Out of total 90 measurement days, March 4, 2015 in winter was the only day that we observed
305 significant nocturnal nucleation. Sunrise and sunset were at 6:29 AM and 18:00 PM local time on
306 March 4, but nucleation were observed persistently from 4:00 AM - 20:00 PM. N_{sub-3} increased from
307 $3.5 \times 10^3 \text{ cm}^{-3}$ at 4:00 AM to $6.3 \times 10^4 \text{ cm}^{-3}$ before sunrise. During 10:00-11:00 AM, peak N_{sub-3}
308 reached $3 \times 10^4 \text{ cm}^{-3}$, 3 times higher than the average of all other event days in winter. Apparently,

309 nocturnal nucleation on March 4 could not be explained as carry-over of daytime particles nor being
310 associated with photochemistry. This implied the existence of certain dark nucleation source. There
311 are a number of observations that have also shown nighttime particle formation events in various
312 atmospheric conditions (Junninen et al., 2008; Lehtipalo et al., 2011; Lee et al., 2008; Ortega et al.,
313 2009, 2012; Russell et al., 2007; Suni et al., 2008; Svenningsson et al., 2008; Yu et al., 2014), but the
314 mechanisms behind the nocturnal nucleation are yet still highly speculative. With our instrument
315 capability in this work, we could not deduce any valuable information on the nocturnal nucleation
316 mechanism, except that we found the air mass on 04 March was relatively clean (both *CS* and gases,
317 mean *CS*: 0.15 s^{-1}), and temperature and RH (mean: 4.4°C and 33%) were favorable for nucleation.

318

319 **3.2 Size- and time dependent formation rates of sub-3 nm particles**

320 We observed 23 Type A events and 9 Type B events during the measurements. The different
321 size distribution patterns (Figure 3) were probably linked to the mechanism or intensity of nucleation
322 and growth. To address this issue, we first compared the formation rates and growth rates in two
323 types of events. Formation rates J of 1.4, 1.6, 1.9, 2.2, 2.4, 2.7 and 3.0 nm particles were shown in
324 Figure 6 (upper panels) for typical Type A and Type B events. It is obvious that $J_{1.4}$ was much higher
325 on February 18 (Type B) than that on May 15 (Type A). A clear time dependence of J was observed.
326 For example, $J_{1.4}$ was $60 \text{ cm}^{-3} \text{ s}^{-1}$ at the onset of the nucleation event on May 15 and increased to 300
327 $\text{cm}^{-3} \text{ s}^{-1}$ in the middle of the day. In the type B event on February 19, the initial and peak $J_{1.4}$ were
328 2.1×10^2 and $1.2 \times 10^3 \text{ cm}^{-3} \text{ s}^{-1}$ respectively. Therefore, our method provided more information of
329 nucleation than conventional calculation methods that usually showed only an averaged J at the onset

330 of a nucleation event. Our method was also different from Kulmala et al. (2013). Their
331 time-dependent formation rate on an event day was equal to size distribution $n(D_p, t)$ times a constant
332 growth rate at the onset of the event obtained with the appearance time method.

333 The diurnal variation of J implied that nucleation was probably linked to sunlight induced
334 photochemistry. We calculated the correlations between $J_{1.4}$ and an H_2SO_4 proxy for the 8 events of
335 our interest. The H_2SO_4 proxy was calculated following $[H_2SO_4] = 8.21 \times 10^{-3} k \cdot Radiation \cdot$
336 $[SO_2]^{0.62} \cdot (CS \cdot RH)^{-0.13}$ (Eq. 8 of Mikkonen et al. 2011), where k is the temperature-dependent
337 reaction-rate constant. Figure 7a show that good linear correlation was usually seen for every single
338 event with R^2 ranging from 0.72 to 0.86 for 6 out of 8 events. A moderate R^2 of 0.56 was obtained
339 for August 15. R^2 was lowest (0.34) on March 4, 2015. This is not surprising because we know
340 March 4 was the only day with nocturnal nucleation during the measurement period. The H_2SO_4
341 proxy was also calculated using the derivation of Petäjä et al. (2009), which resulted in lower R^2 of
342 $\log J_{1.4}$ vs. $\log [H_2SO_4]$ for all 8 events. Therefore, in this study we used Mikkonen H_2SO_4 proxy, as
343 it was derived with more comprehensive datasets than Petäjä et al. (2009). The slopes of $\log J_{1.4}$ vs.
344 $\log [H_2SO_4]$ were close to 1 in all events (0.82-1.17, excluding March 4), indicating activation theory
345 can explain the nucleation mechanism in our urban atmosphere.

346 If data points of all the 8 events were put together, the linear correlation between H_2SO_4 proxy
347 and $J_{1.4}$ deteriorated (slope=1.1, $R^2=0.17$, Figure 7b). In spite of considerable scattering, most of data
348 points located between $J_{1.4}=10^{-4.1} \times [H_2SO_4]$ and $J_{1.4}=10^{-6.3} \times [H_2SO_4]$. An interesting finding was
349 that the scattering of $J_{1.4}$ vs. $[H_2SO_4]$ proxy among all 8 events was probably due to temperature or
350 season change (Figure 7b). More specifically, with the same level of H_2SO_4 proxy, $J_{1.4}$ was higher in

351 winter with lower temperature than in spring/summer with higher temperature. There were two
352 possibilities behind the deteriorated linear correlation between H₂SO₄ proxy and $J_{1,4}$: (1) inaccurate
353 H₂SO₄ proxy and (2) other varying factors in nucleation mechanism. First, it was very likely that
354 H₂SO₄ concentrations in our polluted urban atmosphere were overestimated by the H₂SO₄ proxy of
355 Mikkonen et al. (2011), which was based on statistic regression of historical datasets from relatively
356 clean Europe/USA atmosphere. The extent of overestimation may vary with the levels of predictor
357 variables (e.g., SO₂, temperature, CS). Mean SO₂ mixing ratios were 10.5 and 7.3 ppbv in
358 spring/summer and winter during our measurements, respectively. These were 1 order of magnitude
359 higher than SO₂ mixing ratios at the 6 European and USA sites (mean values: 0.23-3.4 ppbv,
360 Mikkonen et al., 2011). Our CS in the 8 events was on the order of magnitude of 10⁻² s⁻¹, again higher
361 than 10⁻³ s⁻¹ in Mikkonen et al. (2011). Mikkonen et al. (2011) had already pointed out that the
362 predictive ability was lower for long term data due to atmospheric condition changes in different
363 seasons.

364 Second, organic condensing vapor concentrations in particle growth events were higher in winter
365 than those in spring/summer (Table 1, see Section 3.4). If the organics were also involved in
366 nucleation, $J_{1,4}$ should be enhanced in winter. The enhancement of nucleation by organics (most
367 likely anthropogenic organics in our urban atmosphere) could be supported by the comparison of $J_{1,4}$
368 dependences on H₂SO₄ between our study and the measurements in the Boreal forest: besides
369 possible H₂SO₄ overestimation, $J_{1,4}=10^{-4.1} \times [\text{H}_2\text{SO}_4] - 10^{-6.3} \times [\text{H}_2\text{SO}_4]$ in our sites was much higher
370 than $J_{1,5}=1.06 \times 10^{-7} [\text{H}_2\text{SO}_4]^{1.1}$ in Hyytiälä during active aerosol formation periods (Kulmala et al.,

371 2013). At last, low temperature itself might enhance nucleation in winter (Brus et al., 2011) via
372 increasing the saturation ratios of all nucleation precursors (e.g., water, H₂SO₄, organics).

373

374 **3.3 Size- and time dependent growth rates of sub-3 nm particles**

375 Particle size distribution $n(D_p)$ and corresponding $GR(D_p)$ at an instant in time during the events
376 were shown in Figure 6 middle and lower panels. A local minimum of $n(D_p)$ at 2.4 nm, followed by a
377 local maximum somewhere between 2.5 and 10 nm, was seen on May 15, 2014. Such size
378 distribution characteristics on May 15, 2014, as well as on all other Type A event days, was also
379 observed by Kulmala et al. (2013) in the Boreal forest (Figure 1A and S9A in their paper) and by
380 Jiang et al. (2011b) in the urban area of Atlanta, USA (Figure 1 in their paper). We further examined
381 the growth rates in the size range of 1-3 nm on May 15, 2014. It was shown that there was a local
382 maximum of $GR(D_p)$ at 2.4 nm. This could explain why $n(D_p)$ was increasing in 2.4-3 nm size range:
383 when particle condensational flow out of a size bin was slowed down, it was possible that particles
384 flowing into the size bin accumulated, leading to particle number increase in the bin.

385 We saw more unusual behaviors of $n(D_p)$ and $GR(D_p)$ in the Type B event on February 18
386 (Figure 6 right panels): $GR(D_p)$ decreased monotonically in the size range of 1.4 - 3 nm, and
387 accordingly $n(D_p)$ increased monotonically at the same time. A high $GR(D_p)$ of 25 nm h⁻¹ was
388 observed at 1.6 nm and $GR(D_p)$ decreased rapidly to 1.7 nm h⁻¹ at ~3 nm. If we consider that $GR(D_p)$
389 below 1.6 nm would eventually decrease due to strong Kelvin effect of all possible precursors
390 (H₂SO₄ or organics), the overall trend of $GR(D_p)$ in the Type B event was in fact the same as Type A:

391 for the smallest clusters, growth rate was small (possibly below 1 nm h^{-1}) and increased with D_p . It
392 reached a local maximum somewhere between 1-3 nm, after which $GR(D_p)$ decreased with D_p . For a
393 typical NPF event, $GR(D_p)$ would eventually increase again after a local minimum between 3-10 nm.
394 The difference between the Type A event (February 18) and Type B event (May 15) was the D_p of
395 local maximum $GR(D_p)$ (2.4 nm vs. 1.6 nm).

396 The interesting behaviors of $n(D_p)$ and $GR(D_p)$ in our urban atmosphere were different from the
397 stereotyped understanding that steady-state cluster size distribution $n(D_p)$ decreases with D_p in
398 nucleation and GR increases monotonically with D_p in an NPF event. It should be pointed out that if
399 we calculated the overall GR in 1.4-3 nm, $GR_{1.4-3}$ was 3.6 nm h^{-1} on May 15 and 4.4 nm h^{-1} on
400 February 18, which were still smaller than GR_{3-20} during the initial period of the events (7.7 and 6.0
401 nm h^{-1} , calculated using appearance time method). Table 1 showed that a faster GR_{3-20} than $GR_{1.4-3}$
402 were quite common, except in two events on May 16 and 20 when particles did not grow beyond 3
403 nm. Overall, GR was still increasing with increasing D_p .

404 Kuang et al. (2012) had also reported a local maximum of GR at $\sim 2.6 \text{ nm}$ in an NPF event
405 measured in Atlanta, USA (Figure 1b in their paper). In this study we further point out that GR could
406 decrease monotonically with D_p in 1-3 nm range in strong nucleation events. Our GR was calculated
407 from a simplified GDE method, however, the decrease of GR in 1-3 nm size range could be easily
408 inferred from the size spectra shown in Figure 3 or Figure 6 middle panels: for a D_{p2} that was larger
409 than D_{p1} , particle formation rate $J(D_{p2})$ must be smaller than $J(D_{p1})$. If we observed a higher $n(D_{p2})$
410 than $n(D_{p1})$, $GR(D_p)$ that was equal to $J(D_p)/n(D_p)$ must be smaller at D_{p2} than D_{p1} .

411

412 3.4 Growth rate due to condensing organic vapor on newly formed nuclei in sub-3 nm sizes

413 Apparently, the complicated growth rate behaviours in our polluted urban atmosphere can not be
414 explained by H₂SO₄ condensation alone, not only because H₂SO₄ condensational growth rate
415 ($GR_{H_2SO_4}$, calculated from the H₂SO₄ proxy and shown as black dashed lines in Figure 6) was smaller
416 than the measured growth rate (GR_{meas}), but also because $GR_{H_2SO_4}$ curve should follow a
417 monotonically decreasing trend in > 1 nm sizes assuming a collision-only condensational growth
418 without vaporization (Nieminen et al., 2010).

419 Nano-Köhler theory (Anttila et al., 2004; Kulmala et al., 2004b, c) suggested that when a soluble
420 organic vapor is dissolved in newly formed nuclei of aqueous-phase sulfate at certain size between
421 1-3 nm, the surface organic vapor pressure is lowered and thus assists the growth of the nuclei. Here,
422 we continued our discussion based on the nano-Köhler theory to provide an explanation of GR
423 behaviours observed in our urban atmosphere. We first subtract $GR_{H_2SO_4}$ from GR_{meas} to obtain the
424 growth rate due to a condensing organic vapor (hereafter, denoted as ELVOC, extremely low
425 volatility organic compound):

$$GR_{meas,elvoc} = GR_{meas} - GR_{H_2SO_4}$$

426 where $GR_{H_2SO_4}$ is calculated from the H₂SO₄ proxy concentration [H₂SO₄] following Nieminen et al.
427 (2010),:

$$428 \quad GR_{H_2SO_4} = \frac{\gamma}{2\rho_{v,H_2SO_4}} \left(1 + \frac{D_{v,H_2SO_4}}{D_p}\right)^2 \left(\frac{8kT}{\pi}\right)^{\frac{1}{2}} \left(\frac{1}{m_p} + \frac{1}{m_{v,H_2SO_4}}\right)^{\frac{1}{2}} m_{v,H_2SO_4} [H_2SO_4] \quad (4)$$

429 and all parameters in Eq.4 are taken from Nieminen et al. (2010) for H₂SO₄.

430 The size-dependent growth rate due to the uptake of ELVOC was expressed as

431
$$GR_{elvoc} = \frac{\gamma}{2\rho_{v,elvoc}} \left(1 + \frac{D_{v,elvoc}}{D_p}\right)^2 \left(\frac{8kT}{\pi}\right)^{\frac{1}{2}} \left(\frac{1}{m_p} + \frac{1}{m_{v,elvoc}}\right)^{\frac{1}{2}} m_{v,elvoc} (C_{elvoc} - C_{surface}) \quad (5)$$

432 where C_{elvoc} is gas-phase ELVOC concentration far from the particle. The net uptake of
 433 ELVOC is driven by the difference of C_{elvoc} and equilibrium surface concentration over the
 434 particle $C_{surface}$. $C_{surface}$ is determined by the pure component saturation vapor pressure C_{elvoc}^* ,
 435 particle curvature $\exp\left(\frac{4\sigma v}{kTD_p}\right)$ and particle composition:

436
$$C_{surface} = C_{elvoc}^* \exp\left(\frac{4\sigma v}{kTD_p}\right) x_{D_p}$$

437 x_{D_p} is the mole fraction of water-soluble ELVOC in the pseudobinary solution consisting of
 438 ELVOC and the aqueous sulfate nuclei. The pseudobinary solution was treated ideal here. An
 439 example of x_{D_p} as a function of D_p was shown in Figure 8a. Nuclei activation diameter $D_{p,act}$ is the
 440 size that ELVOC fraction begins to increase significantly. For $D_p < D_{p,act}$, x_{D_p} is approximated with
 441 a fixed value (x_0). For $D_p > D_{p,act}$, x_{D_p} increases significantly with the organics being added to the
 442 sulfate core of $D_{p,act}$ size. The size dependent x_{D_p} is approximated as

$$x_{D_p} = \begin{cases} x_0 & , \quad D_p < D_{p,act} \\ x_0 + \frac{(D_p^3 - D_{p,act}^3)/v_{elvoc}}{(D_p^3 - D_{p,act}^3)/v_{elvoc} + D_{p,act}^3/v_{sulfate}} & , \quad D_p \geq D_{p,act} \end{cases}$$

443 Considering strong Kelvin effect, $C_{surface}$ decreases with increasing D_p for $D_p < D_{p,act}$ (Figure
 444 8b dashed black line). For $D_p > D_{p,act}$, the rapidly increasing organic fraction in the small size regime
 445 of 2-3 nm raises the equilibrium $C_{surface}$ of ELVOC first. Then for 3-6 nm particles that are
 446 dominated by organics, $C_{surface}$ decreases to merge with the Kelvin curve of a pure organic droplet
 447 (red line, Figure 8b). The complete equilibrium curve of $C_{surface}$ in 1-6 nm (dashed + solid black

448 lines) was shown in Figure 8c. The blue line represented the calculated $C_{\text{elvoc}} - C_{\text{surface}}$. The trend
 449 of $C_{\text{elvoc}} - C_{\text{surface}}$ coincided with the size dependence of the measured GR corrected by H_2SO_4
 450 ($GR_{\text{meas,elvoc}}$, Figure 8d blue circle). $D_{p,act}$ corresponded to the size with local maximum
 451 $GR_{\text{meas,elvoc}}$.

452 We fitted GR_{elvoc} with $GR_{\text{meas,elvoc}}$ in sub-3 nm sizes at an instant in time by adjusting 3 free
 453 parameters in Eq. (5): x_0 , C_{elvoc} , and C_{elvoc}^* . Other parameters like surface tension (0.02 N m^{-1}) and
 454 molar volume ($135.5 \text{ cm}^3 \text{ mol}^{-1}$) of ELVOC were taken from Kulmala et al. (2004b). Molecule
 455 diameter d_v (0.8 nm) and condensed-phase density ρ_v (1.5 g cm^{-3}) of ELVOC were taken from Ehn
 456 et al. (2014). Uptake coefficient γ was calculated following Nieminen et al. (2010). The fitting
 457 results in Figure 9 showed that the dependence of $GR_{\text{meas,elvoc}}$ on D_p below 3 nm could be well
 458 reproduced by Eq. (5) for both Type A and Type B events. Free parameter x_0 determined the
 459 magnitude of the dashed black line in Figure 8b. x_0 was fitted to be 0.07-0.42 for the 8 events. C_∞
 460 was sensitive to the local maximum $GR_{\text{meas,elvoc}}$ at the $D_{p,act}$. C_{elvoc} , and C_{elvoc}^* determined the
 461 local minimum $GR_{\text{meas,elvoc}}$ at the right side of $D_{p,act}$. Therefore, C^* and C_∞ were basically
 462 determined by the measured GR (local maximum and local minimum) and not sensitive to x_0 . As
 463 shown in Table 1, the condensing organic vapor concentrations C_{elvoc} were $1.7 \times 10^7 - 1.7 \times 10^8 \text{ cm}^{-3}$.
 464 The saturation vapor concentration C_{elvoc}^* were $3.3 \times 10^6 - 5.2 \times 10^7 \text{ cm}^{-3}$. They were within the orders
 465 of magnitude of $10^7 - 10^8 \text{ cm}^{-3}$ and $10^6 - 10^7 \text{ cm}^{-3}$ suggested by Kulmala et al. (2004b), respectively.

466 For comparison, the GR calculated from appearance time method was also shown in Figure 9
 467 (blue cross) for $> 3 \text{ nm}$ particles on May 15, February 18 and February 19, as well as for sub-3 nm
 468 particles on May 20 when particle growth was relatively slow. It can be seen that the GR on May 20

469 calculated from the two methods agreed well with each other, lending credit to our GDE method.
470 The GR in >10 nm sizes was usually underestimated by GR_{elvoc} . This could be interpreted as other
471 condensing vapors with higher volatility may contribute to particle growth in the larger particles. It
472 should be noted that the appearance time method followed the time steps when newly-formed
473 particles appeared in successive size bins and thus the GR calculated from appearance time method
474 as not the growth rates at the same instant in time.

475 For all the 8 nucleation events, Table 1 summarizes the measured values of overall growth rate
476 in 1.4-3 nm ($GR_{1.4-3}$), maximum growth rate in 1.4-3 nm ($GR_{max,1.4-3}$), overall growth rate in 3-20 nm
477 (GR_{3-20}), nucleation rate ($J_{1.4}$), activation diameter ($D_{p,act}$), CS , and temperature (T) during the event
478 periods with maximum nucleation rates. Corresponding estimates of Mikkonen H_2SO_4 proxy, C_{elvoc} ,
479 and C_{elvoc}^* were shown in the right 3 columns. It can be seen that in comparison with more
480 conventional Type A events, Type B events usually occurred with (1) higher $J_{1.4}$, $GR_{max,1.4-3}$, $GR_{1.4-3}$,
481 C_{elvoc} , and CS ; (2) smaller $D_{p,act}$; and (3) lower T . However, the H_2SO_4 proxy and GR_{3-20} were
482 similar in Type A and Type B events. Based on these estimations, we concluded that higher ELVOC
483 concentration C_{elvoc} was the key factor leading to the higher $J_{1.4}$ and $GR_{1.4-3}$, which in turn resulted
484 in the different size spectrum pattern in Type B events (“up-side-down volcano”) from in Type A
485 events (“volcano”).

486 It should be noted that the organic vapor concentrations C_{elvoc} in this study were not directly
487 measured, but estimated based on Eq. (4-5). C_{elvoc} , $[H_2SO_4]$, mole fraction x_{D_p} and growth rates
488 calculated using Eq. (4-5) were for an instant in time. Aerosol dynamic processes, such as nucleation,
489 coagulation, and the condensation growth of H_2SO_4 and water vapor, were not considered explicitly

490 in Eq. (4-5). In addition, bulk thermodynamics was applied in Eq. (5) for extremely small
491 clusters/particles of sub-3 nm sizes. Therefore, although our calculation provided a possibility to
492 explain the size dependence of growth rate observed in the polluted urban atmosphere, C_{elvoc} in this
493 study was subject to uncertainties in (1) the growth rate derived from the GDE method, (2) the theory
494 by which the growth rate was related to the organic vapor concentration, and (3) H_2SO_4 level which
495 was calculated using Mikkonen et al. (2011) proxy.

496

497 **3.5 Inhibited particle growth to CCN-active sizes in strong nucleation events of Type B2**

498 Type B2 was strong nucleation event that produced rather high concentrations of new particles
499 in sub-20 nm size range (Figure 3d). High concentrations of activating vapor in these events (e.g.,
500 C_{∞} : $1.4\text{-}2.0 \times 10^8 \text{ cm}^{-3}$ on February 18 and March 4) should favor a banana-shape NPF event with fast
501 growth of particles >20 nm, due to weakened Kelvin effect. However, it was puzzling to us why new
502 particles accumulated in 2-20 nm and did not grow further on Type B2 event days (see Figure 3d).
503 We first examined the air mass trajectory characteristics of Type B2 events. Compared with Type B1,
504 Type B2 was characterized by long range transport air masses from far north of China and Mongolia.
505 The lumped trajectories with insignificant wind direction change imply that the air mass in Type B2
506 event was quite uniform. In addition, meteorological and chemical variables (high solar radiation
507 flux and wind speed, low temperature, $\text{PM}_{2.5}$, SO_2 , NO_2 , CO and O_3 , green lines in Figure 5)
508 collectively suggested that Type B2 was typical regional event in homogeneous cold air masses.
509 Therefore, the interrupted growth of new particles was not likely to be a result of wind direction
510 change.

511 As seen from Figure 5, meteorological variables on Type B2 days were generally more favorable
512 in aiding particle growth than on Type B1 days: lower PM_{2.5}, lower temperature, and higher solar
513 radiation flux. The unfavorable factors in Type B2 events, however, included lower concentrations of
514 SO₂, NO₂, and CO (anthropogenic emission indicators), lower secondary photochemical product
515 indicators O₃ and lower particle phase sulfate in 100-1000 nm (X. Ge, private communication, 2015,
516 X. Ge conducted simultaneous AMS measurement during our measurement periods). All these
517 evidences suggested that further particle growth in Type B2 events was limited by certain
518 condensing vapor other than ELVOC. Consequently, although there was a pool of sub-20 nm
519 particles, they were not further “activated” due to the low availability of this condensing vapor.
520 Following the terminology of Donahue et al. (2011, 2012), we called this condensing vapor LVOC
521 (low volatility organic compounds)

522 The above hypothesis was sound if we considered that the identity of LVOC for the growth of
523 particles > 20 nm could be different from ELVOC for sub-3 nm particle growth. Hirsikko et al.
524 (2005) observed that GR_{3-20} demonstrated an opposite seasonal cycle to $GR_{1.3-3}$: GR_{3-20} was higher in
525 summer, whereas $GR_{1.3-3}$ was higher in winter. This suggested that the condensing vapors were
526 different in identity for particles of different sizes. Hirsikko et al. (2005) attributed the condensing
527 vapors for GR_{3-20} to biogenetic VOCs. In our urban atmosphere, according to Figure 5, LVOC was
528 more likely to be from anthropogenic sources associated with SO₂, NO_x and CO emissions. A picture
529 of the growth process was thus like this: ELVOC of lower volatility, lower concentration and higher
530 water solubility activated inorganic nuclei and accelerated particle growth in smaller sizes. This in
531 turn assisted in the condensation of LVOC of high volatility, low solubility, but with larger amount

532 of mass. The further growth of particles >20 nm, which means significant increment of particle mass,
533 needed continuous supply of LVOC from the anthropogenic sources. On the Type B2 days, LVOC
534 supply was not adequate (low SO_2 , CO and NO_x). As a result, continuous banana-shape particle
535 growth did not take place.

536 **4. Conclusion**

537 NPF can contribute to CCN only after going through nucleation, initial growth steps and
538 subsequent growth to CCN-active sizes. This study provided the evidences of limiting factors in
539 these processes in a polluted urban atmosphere in China. We observed atmospheric nucleation events
540 on 42 out of total 90 observation days, but particles could grow to CCN-active sizes on only 9 days,
541 which was equivalent to 9 conventional NPF events. In summer, strict emission control measures
542 during the 2014 Youth Olympic Games resulted in relatively low $\text{PM}_{2.5}$ and anthropogenic trace
543 gases (SO_2 , NO_2 , CO and O_3) levels. Infrequent nucleation was thus limited by both low
544 concentrations of gaseous precursors and high temperature and RH in summer. In more polluted
545 winter and spring atmosphere, precursor supply was not limiting anymore; nucleation occurred once
546 meteorological conditions were favorable (i.e. low CS and temperature/RH, higher solar radiation).
547 However, for the further growth of sub-3 nm particles to CCN-active sizes, anthropogenic gaseous
548 precursors again became limiting factors.

549 A simplified GDE method was used in this study to calculate particle formation rates first and
550 then growth rates. Nucleation events were strong in the polluted urban atmosphere of Nanjing. Initial
551 $J_{1.4}$ at the onset and peak $J_{1.4}$ at the noontime could be up to $2.1 \times 10^2 \text{ cm}^{-3} \text{ s}^{-1}$ and $2.5 \times 10^3 \text{ cm}^{-3} \text{ s}^{-1}$,
552 respectively, during the 8 nucleation events selected from different seasons. The diurnal variation of

553 $J_{1.4}$ implied that nucleation was usually linked to sunlight induced photochemistry. Time-dependent
554 $J_{1.4}$ showed good linear correlations with the H_2SO_4 proxy for every single event, except a day with
555 significant nocturnal nucleation. However, the correlation between $J_{1.4}$ and the H_2SO_4 proxy for all 8
556 events deteriorated, which might reflect the effect of temperature or assisting vapor concentration in
557 the nucleation. The deteriorated correlation could also be due to the lower predictive ability of the
558 H_2SO_4 proxy in the polluted urban atmosphere for different seasons.

559 In all nucleation events, a local maximum growth rate was observed between 1-3 nm with GR up
560 to 25 nm h^{-1} . This means GR was not monotonically increasing with particle size. The overall $GR_{1.4-3}$,
561 however, was still smaller than GR_{3-20} , if particles could grow beyond 3 nm. The local maximum
562 growth rate was interpreted as the solvation effect of organic activating vapor in newly formed
563 inorganic nuclei. Based on our estimation, high ELVOC concentration of $2.3 \times 10^7 - 2.0 \times 10^8 \text{ cm}^{-3}$ was
564 expected to be the key factor leading to high $GR_{1.4-3}$. The varying GR of new particle in turn resulted
565 in the different particle growth patterns that we observed in Nanjing.

566 Our results call for a more robust proxy of gaseous H_2SO_4 to be developed for polluted urban
567 conditions. The study also highlighted the importance of estimating or measuring activating organic
568 vapor levels (using CI-APi-TOF, for example) in the initial growth steps of atmospheric NPF. Our
569 year-round measurement data provided valuable size evolution data of sub-3 nm clusters/particles to
570 evaluate previous aerosol dynamic models of new particle formation. A robust dynamic model was
571 needed to appropriately treat all aerosol and gas-phase processes in the initial growth steps.

572

573 **Acknowledgements**

574 This work was supported by National Science Foundation of China (41405116,
575 41275142, 41575122), Natural Science Foundation of Jiangsu Province (BK20140989), and Jiangsu
576 Specially Appointed Professor grant. The measurement campaigns were partially funded by the
577 Priority Academic Program Development of Jiangsu Higher Education Institutions (PAPD). We
578 thank Dr. Vijay P. Kanawade and Dr. Xinlei Ge for valuable discussion.

579

580 **References:**

581 Almeida, J., Schobesberger, S., Kurten, A., Ortega, I. K., Kupiainen-Maatta, O., Praplan, A. P.,
582 Adamov, A., Amorim, A., Bianchi, F., Breitenlechner, M., David, A., Dommen, J., Donahue, N.
583 M., Downard, A., Dunne, E., Duplissy, J., Ehrhart, S., Flagan, R. C., Franchin, A., Guida, R.,
584 Hakala, J., Hansel, A., Heinritzi, M., Henschel, H., Jokinen, T., Junninen, H., Kajos, M.,
585 Kangasluoma, J., Keskinen, H., Kupc, A., Kurten, T., Kvashin, A. N., Laaksonen, A., Lehtipalo,
586 K., Leiminger, M., Leppa, J., Loukonen, V., Makhmutov, V., Mathot, S., McGrath, M. J.,
587 Nieminen, T., Olenius, T., Onnela, A., Petaja, T., Riccobono, F., Riipinen, I., Rissanen, M.,
588 Rondo, L., Ruuskanen, T., Santos, F. D., Sarnela, N., Schallhart, S., Schnitzhofer, R., Seinfeld, J.
589 H., Simon, M., Sipila, M., Stozhkov, Y., Stratmann, F., Tome, A., Trostl, J., Tsagkogeorgas, G.,
590 Vaattovaara, P., Viisanen, Y., Virtanen, A., Vrtala, A., Wagner, P. E., Weingartner, E., Wex, H.,
591 Williamson, C., Wimmer, D., Ye, P., Yli-Juuti, T., Carslaw, K. S., Kulmala, M., Curtius, J.,
592 Baltensperger, U., Worsnop, D. R., Vehkamaki, H., and Kirkby, J.: Molecular understanding of

593 sulphuric acid-amine particle nucleation in the atmosphere, *Nature*, 502(7471), 359-363,
594 doi:10.1038/nature12663, 2013.

595 Anttila, T., Kerminen, V. M., Kulmala, M., Laaksonen, A., and O'Dowd, C. D.: Modelling the
596 formation of organic particles in the atmosphere, *Atmos. Chem. Phys.*, 4(4), 1071-1083, doi:
597 10.5194/acp-4-1071-2004, 2004.

598 Asmi, E., Sipilä M., Manninen, H. E., Vanhanen, J., Lehtipalo, K., Gagné S., Neitola, K., Mirme,
599 A., Mirme, S., Tamm, E., Uin, J., Komsaare, K., Attoui, M., and Kulmala, M.: Results of the first
600 air ion spectrometer calibration and intercomparison workshop, *Atmos. Chem. Phys.*, 9(1),
601 141-154, doi: 10.5194/acp-9-141-2009, 2009.

602 Brus, D., Neitola, K., Hyvärinen, A.-P., Petäjä T., Vanhanen, J., Sipilä M., Paasonen, P., Kulmala,
603 M., and Lihavainen, H.: Homogenous nucleation of sulfuric acid and water at close to
604 atmospherically relevant conditions, *Atmos. Chem. Phys.*, 11(11), 5277-5287, doi:
605 10.5194/acp-11-5277-2011, 2011.

606 Chan, C. K., and Yao, X.: Air pollution in mega cities in China, *Atmos. Environ.*, 42(1), 1-42,
607 doi: :10.1016/j.atmosenv.2007.09.003.

608 Donahue, N. M., Trump, E. R., Pierce, J. R., and Riipinen, I.: Theoretical constraints on pure
609 vapor-pressure driven condensation of organics to ultrafine particles, *Geophys. Res. Lett.*, 38(16),
610 L16801, doi: 10.1029/2011gl048115, 2011.

611 Donahue, N. M., Kroll, J. H., Pandis, S. N., and Robinson, A. L.: A two-dimensional volatility basis
612 set – Part 2: Diagnostics of organic-aerosol evolution, *Atmos. Chem. Phys.*, 12(2), 615-634, doi:
613 10.5194/acp-12-615-2012, 2012.

614 Ehn, M., Thornton, J. A., Kleist, E., Sipila, M., Junninen, H., Pullinen, I., Springer, M., Rubach, F.,
615 Tillmann, R., Lee, B., Lopez-Hilfiker, F., Andres, S., Acir, I.-H., Rissanen, M., Jokinen, T.,
616 Schobesberger, S., Kangasluoma, J., Kontkanen, J., Nieminen, T., Kurten, T., Nielsen, L. B.,
617 Jorgensen, S., Kjaergaard, H. G., Canagaratna, M., Maso, M. D., Berndt, T., Petaja, T., Wahner,
618 A., Kerminen, V. M., Kulmala, M., Worsnop, D. R., Wildt, J., and Mentel, T. F.: A large source
619 of low-volatility secondary organic aerosol, *Nature*, 506(7489), 476-479, doi:
620 10.1038/nature13032, 2014.

621 Herrmann, E., Ding, A. J., Kerminen, V.-M., Petäjä T., Yang, X. Q., Sun, J. N., Qi, X. M.,
622 Manninen, H., Hakala, J., Nieminen, T., Aalto, P. P., Kulmala, M., and Fu, C. B.: Aerosols and
623 nucleation in eastern China: first insights from the new SORPES-NJU station, *Atmos. Chem.*
624 *Phys.*, 14, 2169-2183, doi: 10.5194/acp-14-2169-2014, 2014.

625 Hirsikko, A., Laakso, L., Horrak, U., Aalto, P. P., Kerminen, V. M., and Kulmala, M.: Annual and
626 size dependent variation of growth rates and ion concentrations in boreal forest, *Boreal Environ.*
627 *Res.*, 10, 357-469, 2005.

628 Jiang, J., Chen, M., Kuang, C., Attoui, M., and McMurry, P. H.: Electrical Mobility Spectrometer
629 Using a Diethylene Glycol Condensation Particle Counter for Measurement of Aerosol Size

630 Distributions Down to 1 nm, *Aerosol Sci. Technol.*, 45(4), 510-521, doi:
631 10.1080/02786826.2010.547538, 2011a.

632 Jiang, J., Zhao, J., Chen, M., Eisele, F. L., Scheckman, J., Williams, B. J., Kuang, C., and McMurry,
633 P. H.: First Measurements of Neutral Atmospheric Cluster and 1-2 nm Particle Number Size
634 Distributions During Nucleation Events, *Aerosol Sci. Technol.*, 45(4), II-V, doi:
635 10.1080/02786826.2010.546817, 2011b.

636 Jokinen, T., Sipilä M., Junninen, H., Ehn, M., Lönn, G., Hakala, J., Petäjä T., Mauldin III, R. L.,
637 Kulmala, M., and Worsnop, D. R.: Atmospheric sulphuric acid and neutral cluster measurements
638 using CI-API-TOF, *Atmos. Chem. Phys.*, 12(9), 4117-4125, doi: 10.5194/acp-12-4117-2012,
639 2012.

640 Junninen, H., Hulkkonen, M., Riipinen, I., Nieminen, T., Hirsikko, A., Suni, T., Boy, M., Lee, S.-H.,
641 Vana, M., Tammet, T., Kerminen, V. M., and Kulmala, M.: Observations on nocturnal growth of
642 atmospheric clusters, *Tellus Ser. B*, 60, 365-371, doi:10.1111/j.1600-0889.2008.00356.x, 2008.

643 Junninen, H., Ehn, M., Petäjä T., Luosujärvi, L., Kotiaho, T., Kostianen, R., Rohner, U., Gonin, M.,
644 Fuhrer, K., Kulmala, M., and Worsnop, D. R.: A high-resolution mass spectrometer to measure
645 atmospheric ion composition, *Atmos. Meas. Tech.*, 3, 1039-1053, doi: 10.5194/amtd-3-599-2010,
646 2010.

647 Kangasluoma, J., Kuang, C., Wimmer, D., Rissanen, M. P., Lehtipalo, K., Ehn, M., Worsnop, D.R.,
648 Wang, J., Kulmala, M. and Petäjä T.: Sub-3 nm particle size and composition dependent

649 response of a nano-CPC battery. *Atmos. Meas. Tech.*, 7, 689-700, doi: 10.5194/amt-7-689-2014,
650 2014.

651 Kirkby, J., Curtius, J., Almeida, J., Dunne, E., Duplissy, J., Ehrhart, S., Franchin, A., Gagne, S.,
652 Ickes, L., Kurten, A., Kupc, A., Metzger, A., Riccobono, F., Rondo, L., Schobesberger, S.,
653 Tsagkogeorgas, G., Wimmer, D., Amorim, A., Bianchi, F., Breitenlechner, M., David, A.,
654 Dommen, J., Downard, A., Ehn, M., Flagan, R. C., Haider, S., Hansel, A., Hauser, D., Jud, W.,
655 Junninen, H., Kreissl, F., Kvashin, A., Laaksonen, A., Lehtipalo, K., Lima, J., Lovejoy, E. R.,
656 Makhmutov, V., Mathot, S., Mikkila, J., Minginette, P., Mogo, S., Nieminen, T., Onnela, A.,
657 Pereira, P., Petaja, T., Schnitzhofer, R., Seinfeld, J. H., Sipila, M., Stozhkov, Y., Stratmann, F.,
658 Tome, A., Vanhanen, J., Viisanen, Y., Virtala, A., Wagner, P. E., Walther, H., Weingartner, E.,
659 Wex, H., Winkler, P. M., Carslaw, K. S., Worsnop, D. R., Baltensperger, U., and Kulmala, M.:
660 Role of sulphuric acid, ammonia and galactic cosmic rays in atmospheric aerosol nucleation,
661 *Nature*, 476(7361), 429-433, doi:10.1038/nature10343, 2011.

662 Kuang, C., Chen, M., Zhao, J., Smith, J., McMurry, P. H., and Wang, J.: Size- and time-resolved
663 growth rate measurements of 1 to 5 nm freshly formed atmospheric nuclei, *Atmos. Chem. Phys.*,
664 12(9), 3573-3589, doi: 10.5194/acpd-11-25427-2011, 2012.

665 Kulmala, M., Pirjola, L., and Makela, J. M.: Stable sulfate clusters as a source of new atmospheric
666 particles, *Nature*, 404, 60-66, doi: 10.1038/35003550, 2000.

667 Kulmala, M., Laakso, L., Lehtinen, K. E. J., Riipinen, I., Dal Maso, M., Lauria, A., Kerminen, V. M.,
668 Birmili, W., McMurry, P.H.: Formation and growth rates of ultrafine atmosphere particles: A
669 review of observations, *J. Aerosol. Sci.*, 35, 143-176, 2004a.

670 Kulmala, M., Kerminen, V. M., Anntila, T., Laaksonen, A., and O'Dowd, C. D.: Organic aerosol
671 formation via sulfate cluster activation, *J. Geophys. Res.*, 109, D04205, doi:
672 10.1029/2003JD003961, 2004b.

673 Kulmala, M., Laakso, L., Lehtinen, K. E. J., Riipinen, I., Dal Maso, M., Anttila, T., Kerminen, V.-M.,
674 Hõrrak, U., Vana, M., and Tammet, H.: Initial steps of aerosol growth, *Atmos. Chem. Phys.*,
675 4(11), 2553-2560, doi: 10.5194/acp-4-2553-2004, 2004c.

676 Kulmala, M., Petäjä T., Nieminen, T., Sipilä M., Manninen, H. E., Lehtipalo, K., Dal Maso, M.,
677 Aalto, P. P., Junninen, H., Paasonen, P., Riipinen, I., Lehtinen, K. E. J., Laaksonen, A., and
678 Kerminen, V. M.: Measurement of the nucleation of atmospheric aerosol particles, *Nat. Protocols*,
679 7(9), 1651-1667, doi: 10.1038/nprot.2012.091, 2012.

680 Kulmala, M., Kontkanen, J., Junninen, H., Lehtipalo, K., Manninen, H. E., Nieminen, T., Petäjä T.,
681 Sipilä M., Schobesberger, S., Rantala, P., Franchin, A., Jokinen, T., Järvinen, E., Äijälä M.,
682 Kangasluoma, J., Hakala, J., Aalto, P. P., Paasonen, P., Mikkilä J., Vanhanen, J., Aalto, J.,
683 Hakola, H., Makkonen, U., Ruuskanen, T., Mauldin, R. L., Duplissy, J., Vehkamäki, H., Bäck, J.,
684 Kortelainen, A., Riipinen, I., Kurtén, T., Johnston, M. V., Smith, J. N., Ehn, M., Mentel, T. F.,
685 Lehtinen, K. E. J., Laaksonen, A., Kerminen, V. M., and Worsnop, D. R.: Direct Observations of

686 Atmospheric Aerosol Nucleation, *Science*, 339(6122), 943-946, doi: 10.1126/science.1227385,
687 2013.

688 Kulmala, M., Petäjä T., Ehn, M., Thornton, J., Sipilä M., Worsnop, D. R. and Kerminen, V. M.:
689 Chemistry of Atmospheric Nucleation: On the Recent Advances on Precursor Characterization
690 and Atmospheric Cluster Composition in Connection with Atmospheric New Particle Formation,
691 *Annu. Rev. Phys. Chem.*, 65, 21–37, doi: 10.1146/annurev-physchem-040412-110014, 2014.

692 Kürten, A., Jokinen, T., Simon, M., Sipilä M., Sarnela, N., Junninen, H., Adamov, A., Almeida, J.,
693 Amorim, A., Bianchi, F., Breitenlechner, M., Dommen, J., Donahue, N. M., Duplissy, J., Ehrhart,
694 S., Flagan, R. C., Franchin, A., Hakala, J., Hansel, A., Heinritzi, M., Hutterli, M., Kangasluoma,
695 J., Kirkby, J., Laaksonen, A., Lehtipalo, K., Leiminger, M., Makhmutov, V., Mathot, S., Onnela,
696 A., Petäjä T., Praplan, A. P., Riccobono, F., Rissanen, M. P., Rondo, L., Schobesberger, S.,
697 Seinfeld, J. H., Steiner, G., Tomé A., Tröstl, J., Winkler, P. M., Williamson, C., Wimmer, D., Ye,
698 P., Baltensperger, U., Carslaw, K. S., Kulmala, M., Worsnop, D. R., and Curtius, J.: Neutral
699 molecular cluster formation of sulfuric acid–dimethylamine observed in real time under
700 atmospheric conditions, *Proc. Natl. Acad. Sci. U.S.A.*, 111(42), 15019-15024,
701 doi:10.1073/pnas.1404853111, 2014.

702 Lee, S. H., Young, L. H., Benson, D. R., Kulmala, M., Junninen, H., Suni, T., Campos, T., Rogers, D.
703 C., and Jensen, J.: Observations of nighttime new particle formation in the troposphere, *J.*
704 *Geophys. Res.*, 113, D10210, doi: 10.1029/12007JD009351, 2008.

705 Lehtipalo, K., Sipil ä M., Riipinen, I., Nieminen, T., and Kulmala, M.: Analysis of atmospheric
706 neutral and charged molecular clusters in boreal forest using pulse-height CPC, *Atmos. Chem.*
707 *Phys.*, 9, 4177–4184, 2009.

708 Lehtipalo, K., Sipila, M., Junninen, H., Ehn, M., Berndt, T., Kajos, M. K., Worsnop, D. R., Petaja, T.,
709 and Kulmala, M.: Nanoparticles in boreal forest and coastal environment: a comparison of
710 observations and implications of the nucleation mechanism, *Atmos. Chem. Phys.*, 10, 7009-7016,
711 2010.

712 Lehtipalo, K., Sipila, M., Junninen, H., Ehn, M., Berndt, T., Kajos, M. K., Worsnop, D. R., Petaja, T.,
713 and Kulmala, M.: Observations of Nano-CN in the Nocturnal Boreal Forest, *Aerosol Sci.*
714 *Technol.*, 45(4), 499-509, doi: 10.1080/02786826.2010.547537, 2011.

715 Lehtipalo., K., Lepp ä, J., Kontkanen., J., Kangasluoma., J., Franchin., A., Wimmer., D.,
716 Schobesberger., S., Junninen., H., Pet ä ä, T., Sipil ä, M., Mikkil ä, J., Vanhanen., J., Worsnop., D.
717 R., and Kulmala, M.: Methods for determining particle size distribution and growth rates between
718 1 and 3 nm using the Particle Size Magnifier, *Boreal Environ. Res.*, 19, 215–236, 2014.

719 Matsui, H., Koike, M., Takegawa, N., Kondo, Y., Takami, A., Takamura, T., Yoon, S., Kim, S. W.,
720 Lim, H. C., and Fast, J. D.: Spatial and temporal variations of new particle formation in East Asia
721 using an NPF-explicit WRF-chem model: North-south contrast in new particle formation
722 frequency, *J. Geophys. Res.*, 118(20), 11,647-611,663, doi:10.1002/jgrd.50821, 2013.

723 Merikanto, J., Spracklen, D. V., Mann, G. W., Pickering, S. J., and Carslaw, K. S.: Impact of
724 nucleation on global CCN, *Atmos. Chem. Phys.*, doi: 10.5194/acp-9-8601-2009, 9, 8601-8616,
725 2009.

726 Mikkonen, S., Romakkaniemi, S., Smith, J. N., Korhonen, H., Petäjä T., Plass-Duelmer, C., Boy, M.,
727 McMurry, P. H., Lehtinen, K. E. J., Joutsensaari, J., Hamed, A., Mauldin III, R. L., Birmili, W.,
728 Spindler, G., Arnold, F., Kulmala, M., and Laaksonen, A.: A statistical proxy for sulphuric acid
729 concentration, *Atmos. Chem. Phys.*, 11:11319-11334, doi: 10.5194/acpd-11-20141-2011, 2011.

730 Nieminen, T., Lehtinen, K. E. J., and Kulmala, M.: Sub-10 nm particle growth by vapor
731 condensation - effects of vapor molecule size and particle thermal speed, *Atmos. Chem. Phys.*,
732 10(20), 9773-9779, doi: 10.5194/acp-10-9773-2010, 2010.

733 Ortega, I. K., Suni, T., Gronholm, T., Boy, M., Hakola, H., Hellen, H., Valmari, T., Arvela, H.,
734 Vehkamäki, H., and Kulmala, M.: Is eucalyptol the cause of nocturnal events observed in
735 Australia?, *Boreal Environ. Res.*, 14(4), 606-615, 2009.

736 Ortega, I. K., Suni, T., Boy, M., Grönholm, T., Manninen, H. E., Nieminen, T., Ehn, M., Junninen,
737 H., Hakola, H., Hellén, H., Valmari, T., Arvela, H., Zegelin, S., Hughes, D., Kitchen, M., Cleugh,
738 H., Worsnop, D. R., Kulmala, M., and Kerminen, V. M.: New insights into nocturnal nucleation,
739 *Atmos. Chem. Phys.*, 12(9), 4297-4312, doi:10.5194/acp-12-4297-2012, 2012.

740 Petäjä T., Mauldin, III, R. L., Kosciuch, E., McGrath, J., Nieminen, T., Paasonen, P., Boy, M.,
741 Adamov, A., Kotiaho, T., and Kulmala, M.: Sulfuric acid and OH concentrations in a boreal
742 forest site, *Atmos. Chem. Phys.*, 9, 7435–7448, doi:10.5194/acp-9-7435-2009, 2009.

743 Pierce, J. R., and Adams, P. J.: Uncertainty in global CCN concentrations from uncertain aerosol
744 nucleation and primary emission rates, *Atmos. Chem. Phys.*, 9(4), 1339-1356, doi:
745 10.5194/acp-9-1339-2009, 2009.

746 Riccobono, F., Schobesberger, S., Scott, C. E., Dommen, J., Ortega, I. K., Rondo, L., Almeida, J.,
747 Amorim, A., Bianchi, F., Breitenlechner, M., David, A., Downard, A., Dunne, E. M., Duplissy, J.,
748 Ehrhart, S., Flagan, R. C., Franchin, A., Hansel, A., Junninen, H., Kajos, M., Keskinen, H., Kupc,
749 A., Kürten, A., Kvashin, A. N., Laaksonen, A., Lehtipalo, K., Makhmutov, V., Mathot, S.,
750 Nieminen, T., Onnela, A., Petäjä T., Praplan, A. P., Santos, F. D., Schallhart, S., Seinfeld, J. H.,
751 Sipilä M., Spracklen, D. V., Stozhkov, Y., Stratmann, F., Tomé A., Tsagkogeorgas, G.,
752 Vaattovaara, P., Viisanen, Y., Vrtala, A., Wagner, P. E., Weingartner, E., Wex, H., Wimmer, D.,
753 Carslaw, K. S., Curtius, J., Donahue, N. M., Kirkby, J., Kulmala, M., Worsnop, D. R., and
754 Baltensperger, U.: Oxidation Products of Biogenic Emissions Contribute to Nucleation of
755 Atmospheric Particles, *Science*, 344(6185), 717-721, doi:10.1126/science.1243527, 2014.

756 Riipinen, I., Yli-Juuti, T., Pierce, J. R., Petaja, T., Worsnop, D. R., Kulmala, M., and Donahue, N.
757 M.: The contribution of organics to atmospheric nanoparticle growth, *Nature Geosci.*, 5(7),
758 453-458, doi: 10.1038/NGEO1499, 2012.

759 Russell, L. M., Mensah, A. A., Fischer, E. V., Sive, B. C., Varner, R. K., Keene, W. C., Stutz, J., and
760 Pszenny, A. A. P.: Nanoparticle growth following photochemical α - and β -pinene oxidation at
761 Appledore Island during International Consortium for Research on Transport and
762 Transformation/Chemistry of Halogens at the Isles of Shoals 2004, *J. Geophys. Res.*, 112(D10),
763 D10S21, doi:10.1029/2006jd007736, 2007. Seinfeld, J. H., and Pandis, S. N.: Atmospheric

764 chemistry and physics: from air pollution to climate change, 2nd ed., John Wiley and Sons. Inc.,
765 New York, 2006.

766 Schobesberger, S., Junninen, H., Bianchi, F., Lönn, G., Ehn, M., Lehtipalo, K., Dommen, J., Ehrhart,
767 S., Ortega, I. K., Franchin, A., Nieminen, T., Riccobono, F., Hutterli, M., Duplissy, J., Almeida,
768 J., Amorim, A., Breitenlechner, M., Downard, A. J., Dunne, E. M., Flagan, R. C., Kajos, M.,
769 Keskinen, H., Kirkby, J., Kupc, A., Kürten, A., Kurtén, T., Laaksonen, A., Mathot, S., Onnela, A.,
770 Praplan, A. P., Rondo, L., Santos, F. D., Schallhart, S., Schnitzhofer, R., Sipilä M., Tomé A.,
771 Tsagkogeorgas, G., Vehkamäki, H., Wimmer, D., Baltensperger, U., Carslaw, K. S., Curtius, J.,
772 Hansel, A., Petäjä T., Kulmala, M., Donahue, N. M., and Worsnop, D. R.: Molecular
773 understanding of atmospheric particle formation from sulfuric acid and large oxidized organic
774 molecules, *Proc. Natl. Acad. Sci. U.S.A.*, doi:10.1073/pnas.1306973110, 2013.

775 Sipilä, M., Lehtipalo, K., Attoui, M., Neitola, K., Petäjä T., Aalto, P. P., O'Dowd, C. D., and
776 Kulmala, M.: Laboratory Verification of PH-CPC's Ability to Monitor Atmospheric Sub-3 nm
777 Clusters, *Aerosol Sci. Technol.*, 43(2), 126-135, doi: 10.1080/02786820802506227, 2009.

778 Spracklen, D. V., Carslaw, K. S., Kulmala, M., Kerminen, V.-M., Sihto, S.-L., Riipinen, I.,
779 Merikanto, J., Mann, G. W., Chipperfield, M. P., Wiedensohler, A., Birmili, W., and Lihavainen,
780 H.: Contribution of particle formation to global cloud condensation nuclei concentrations,
781 *Geophys. Res. Lett.*, 35(6), L06808, doi:10.1029/2007GL033038, 2008.

782 Suni, T., Kulmala, M., Hirsikko, A., Bergman, T., Laakso, L., Aalto, P. P., Leuning, R., Cleugh, H.,
783 Zegelin, S., Hughes, D., van Gorsel, E., Kitchen, M., Vana, M., Hõrrak, U., Mirme, S., Mirme, A.,

784 Sevanto, S., Twining, J., and Tadros, C.: Formation and characteristics of ions and charged
785 aerosol particles in a native Australian Eucalypt forest, *Atmos. Chem. Phys.*, 8(1), 129-139,
786 doi:10.5194/acp-8-129-2008, 2008.

787 Svenningsson, B., Arneth, A., Hayward, S., Holst, T., Massling, A., Swietlicko, E., Hirsikko, A.,
788 Junninen, H., Riipinen, I., Vana, M., Dal Maso, M., Hussein, T., and Kulmala, M.: Aerosol
789 particle formation events and analysis of high growth rates observed above a subarctic
790 wetland-forest mosaic, *Tellus*, 60(B), 353-365, doi:10.1111/j.1600-0889.2008.00351.x, 2008.

791 Vanhanen, J., Mikkilä, J., Lehtipalo, K., Sipilä, M., Manninen, H. E., Siivola, E., Petaja, T., and
792 Kulmala, M.: Particle Size Magnifier for Nano-CN Detection, *Aerosol Sci. Technol.*, 45(4),
793 533-542, doi: 10.1080/02786826.2010.547889, 2011.

794 von der Weiden, S. L., Drewnick, F., and Borrmann, S.: Particle Loss Calculator – a new software
795 tool for the assessment of the performance of aerosol inlet systems, *Atmos. Meas. Tech.*, 2(2),
796 479-494, doi: 10.5194/amt-2-479-2009, 2009.

797 Wiedensohler, A., Cheng, Y. F., Nowak, A., Wehner, B., Achtert, P., Berghof, M., Birmili, W., Wu,
798 Z. J., Hu, M., Zhu, T., Takegawa, N., Kita, K., Kondo, Y., Lou, S. R., Hofzumahaus, A., Holland,
799 F., Wahner, A., Gunthe, S. S., Rose, D., Su, H., and Pöschl, U.: Rapid aerosol particle growth and
800 increase of cloud condensation nucleus activity by secondary aerosol formation and condensation:
801 A case study for regional air pollution in northeastern China, *J. Geophys. Res.*, 114(D2), D00G08,
802 doi:10.1029/2008jd010884, 2009.

803 Wang, J., and Wexler, A. S.: Adsorption of organic molecules may explain growth of newly
804 nucleated clusters and new particle formation, *Geophys. Res. Lett.*, 11, 2834-2838, doi:
805 10.1002/grl.50455, 2013.

806 Wang, J., McGraw, R. L., and Kuang, C.: Growth of atmospheric nano-particles by heterogeneous
807 nucleation of organic vapor, *Atmos. Chem. Phys.*, 13(13), 6523-6531, doi:
808 10.5194/acp-13-6523-2013, 2013.

809 Xiao, S., Wang, M. Y., Yao, L., Kulmala, M., Zhou, B., Yang, X., Chen, J. M., Wang, D. F., Fu, Q.
810 Y., Worsnop, D. R., and Wang, L.: Strong atmospheric new particle formation in winter in urban
811 Shanghai, China, *Atmos. Chem. Phys.*, 15(4), 1769-1781, doi: 10.5194/acp-15-1769-2015, 2015.

812 Yu, H., Gannet Hallar, A., You, Y., Sedlacek, A., Springston, S., Kanawade, V. P., Lee, Y. N., Wang,
813 J., Kuang, C., McGraw, R. L., McCubbin, I., Mikkilä J., and Lee, S. H.: Sub-3 nm particles
814 observed at the coastal and continental sites in the United States, *J. Geophys. Res.*, 119(2),
815 2013JD020841, doi: 10.1002/2013jd020841, 2014a.

816 Yu, H., Ortega, J., Smith, J. N., Guenther, A. B., Kanawade, V. P., You, Y., Liu, Y., Hosman, K.,
817 Karl, T., Seco, R., Geron, C., Pallardy, S. G., Gu, L., Mikkilä J., and Lee, S. H.: New Particle
818 Formation and Growth in an Isoprene-Dominated Ozark Forest: From Sub-5 nm to CCN-Active
819 Sizes, *Aerosol Sci. Technol.*, 48(12), 1285-1298, doi: 10.1080/02786826.2014.984801, 2014b.

820 Yu, F., and Luo, G.: Simulation of particle size distribution with a global aerosol model: contribution
821 of nucleation to aerosol and CCN number concentrations, *Atmos. Chem. Phys.*, 9(20), 7691-7710,
822 doi:10.5194/acp-9-7691-2009, 2009.

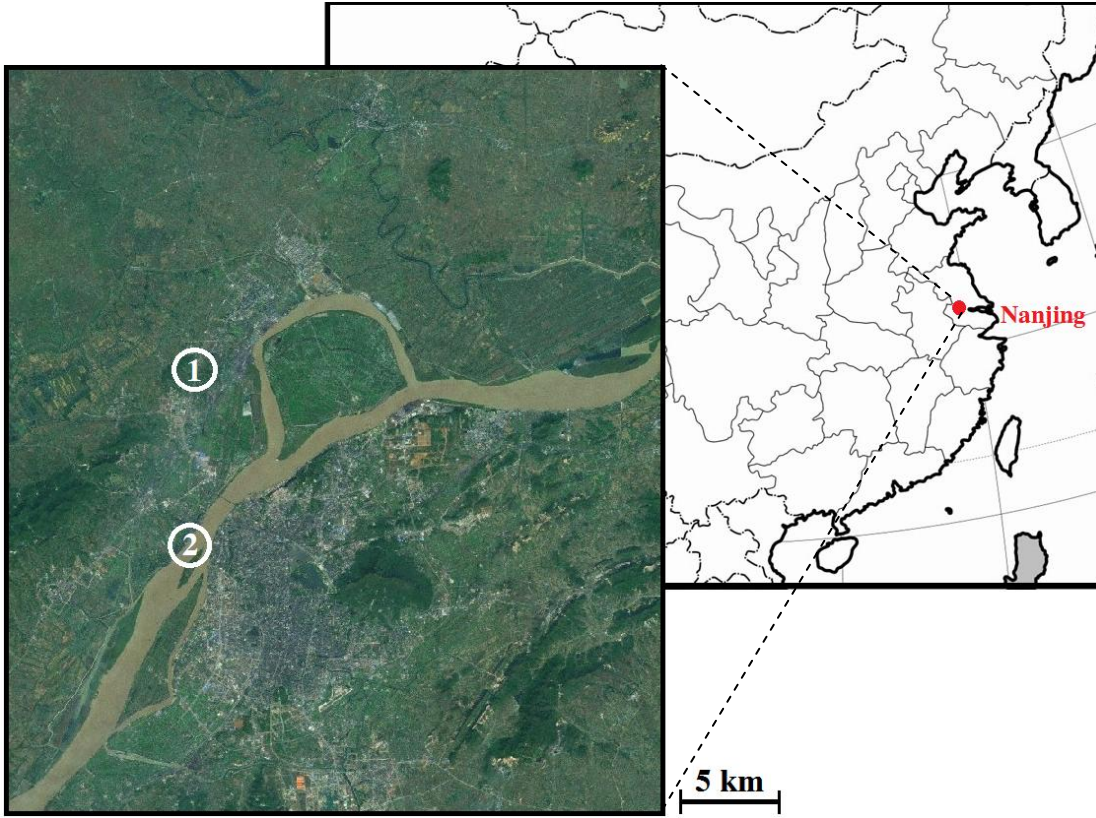
823 Yue, D. L., Hu, M., Zhang, R. Y., Wu, Z. J., Su, H., Wang, Z. B., Peng, J. F., He, L. Y., Huang, X. F.,
824 Gong, Y. G., and Wiedensohler, A.: Potential contribution of new particle formation to cloud
825 condensation nuclei in Beijing, *Atmos. Environ.*, 45(33), 6070-6077,
826 doi:10.1016/j.atmosenv.2011.07.037, 2011.

827 Zhang, K. M., and Wexler, A. S.: A hypothesis for growth of fresh atmospheric nuclei, *J. Geophys.*
828 *Res.*, 107, 4577, doi: 10.1029/2002JD002180, 2002.

829 Zhao, J., Eisele, F. L., Titcombe, M., Kuang, C., and McMurry, P. H.: Chemical ionization mass
830 spectrometric measurements of atmospheric neutral clusters using the cluster-CIMS, *J. Geophys.*
831 *Res.*, 115, D08205, doi: 10.1029/2009JD012606, 2010.

832 Table 1. Activation diameter ($D_{p,act}$), maximum growth rate in 1.4-3 nm ($GR_{max, 1.4-3}$), overall growth rate in 1.4-3 nm ($GR_{1.4-3}$), overall growth
833 rate in 3-20 nm (GR_{3-20}), nucleation rate ($J_{1.4}$), condensation sink (CS), and temperature (T) of selected nucleation events. Estimated gas-phase
834 condensing vapor concentrations C_{elvoc} , pure saturation concentration of condensing vapor over flat surface C_{elvoc}^* , and Mikkonen H₂SO₄ proxy
835 were shown in right 3 columns. All data were for the time periods with maximum nucleation rates.

Type	Date	$D_{p,act}$ (nm)	$GR_{max,1.4-3}$ (nm h ⁻¹)	$GR_{1.4-3}$ (nm h ⁻¹)	GR_{3-20} (nm h ⁻¹)	$J_{1.4}$ (cm ⁻³ s ⁻¹)	T (°C)	CS (10 ⁻² s ⁻¹)	Mikkonen H ₂ SO ₄ proxy (cm ⁻³)	C_{elvoc} (cm ⁻³)	C_{elvoc}^* (cm ⁻³)
A1	May 15, 2014	2.4	6.4	3.6	7.7	3.0×10 ²	20.8	1.6	2.9×10 ⁷	3.5×10 ⁷	6.3×10 ⁶
A1	Aug 15, 2014	2.4	14.5	7.1	7.7	2.0×10 ²	26.1	1.8	3.1×10 ⁷	8.5×10 ⁷	2.1×10 ⁷
A2	May 16, 2014	2.4	3.8	1.9	0	95	25.3	1.9	1.4×10 ⁷	2.5×10 ⁷	4.6×10 ⁶
A2	May 20, 2014	2.2	2.9	1.6	0	92	24.1	1.9	1.3×10 ⁷	1.7×10 ⁷	3.3×10 ⁶
B1	Feb 18, 2015	1.6	25.9	4.4	6.0	1.1×10 ³	8.2	3.3	3.9×10 ⁷	1.4×10 ⁸	3.0×10 ⁷
B1	Dec 27, 2014	1.6	17.7	4.2	5.5	1.9×10 ²	7.6	2.8	3.5×10 ⁷	1.1×10 ⁸	2.2×10 ⁷
B2	Feb 19, 2015	1.9	25.0	8.9	10.1	8.0×10 ²	7.4	3.2	3.7×10 ⁷	1.7×10 ⁸	5.2×10 ⁷
B2	Mar 4, 2015	1.9	18.0	5.8	8.7	2.5×10 ³	3.9	2.2	4.8×10 ⁷	1.3×10 ⁸	1.1×10 ⁷



836

837

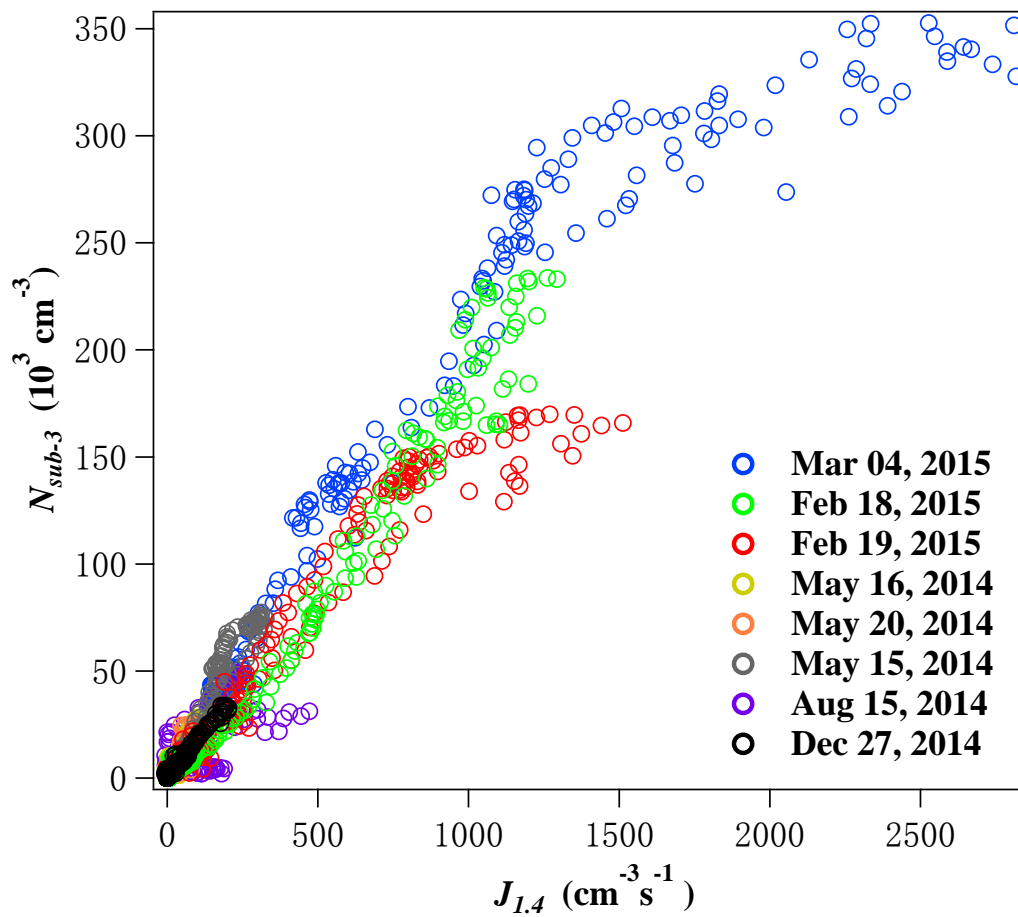
838

839

840

Figure 1. Locations of two urban measurement sites in Nanjing, the second largest megacity in the Yangtze River Delta region, China. ① is the NUIST site and ② is the summer measurement site.

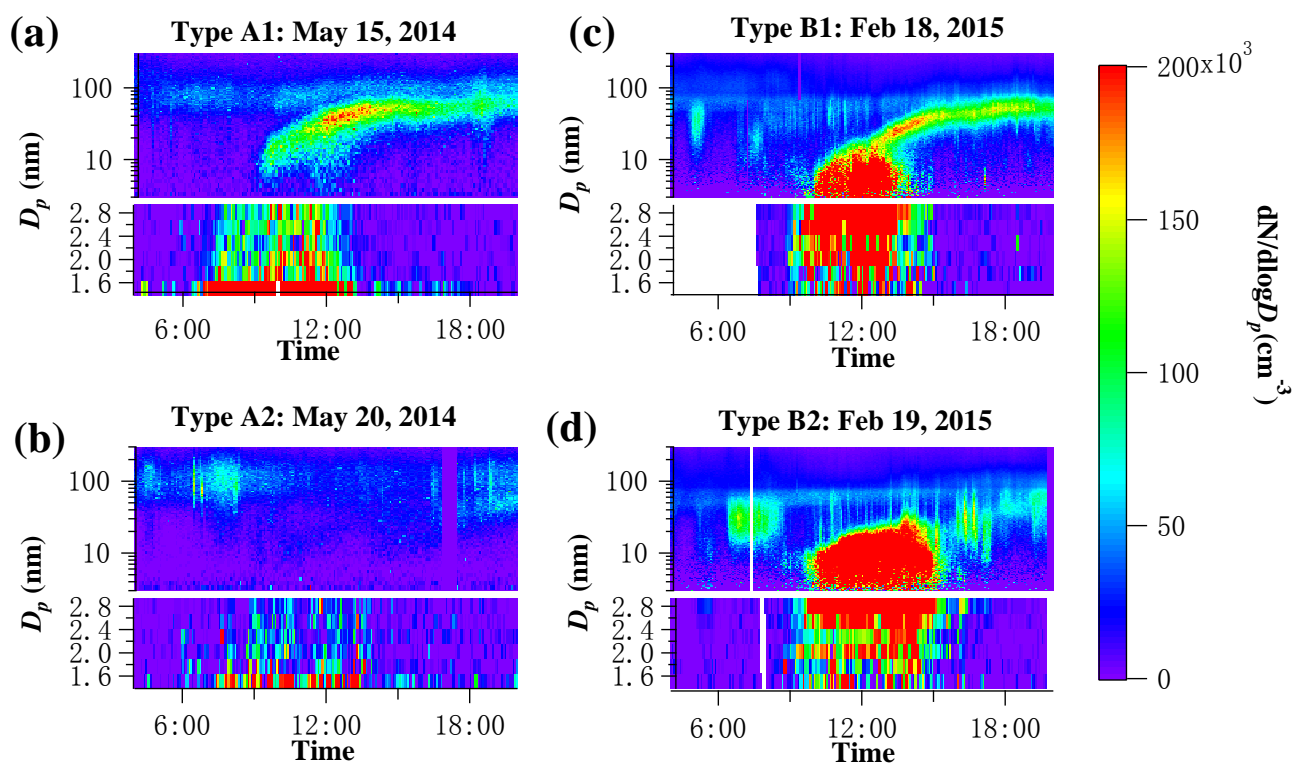
841



842

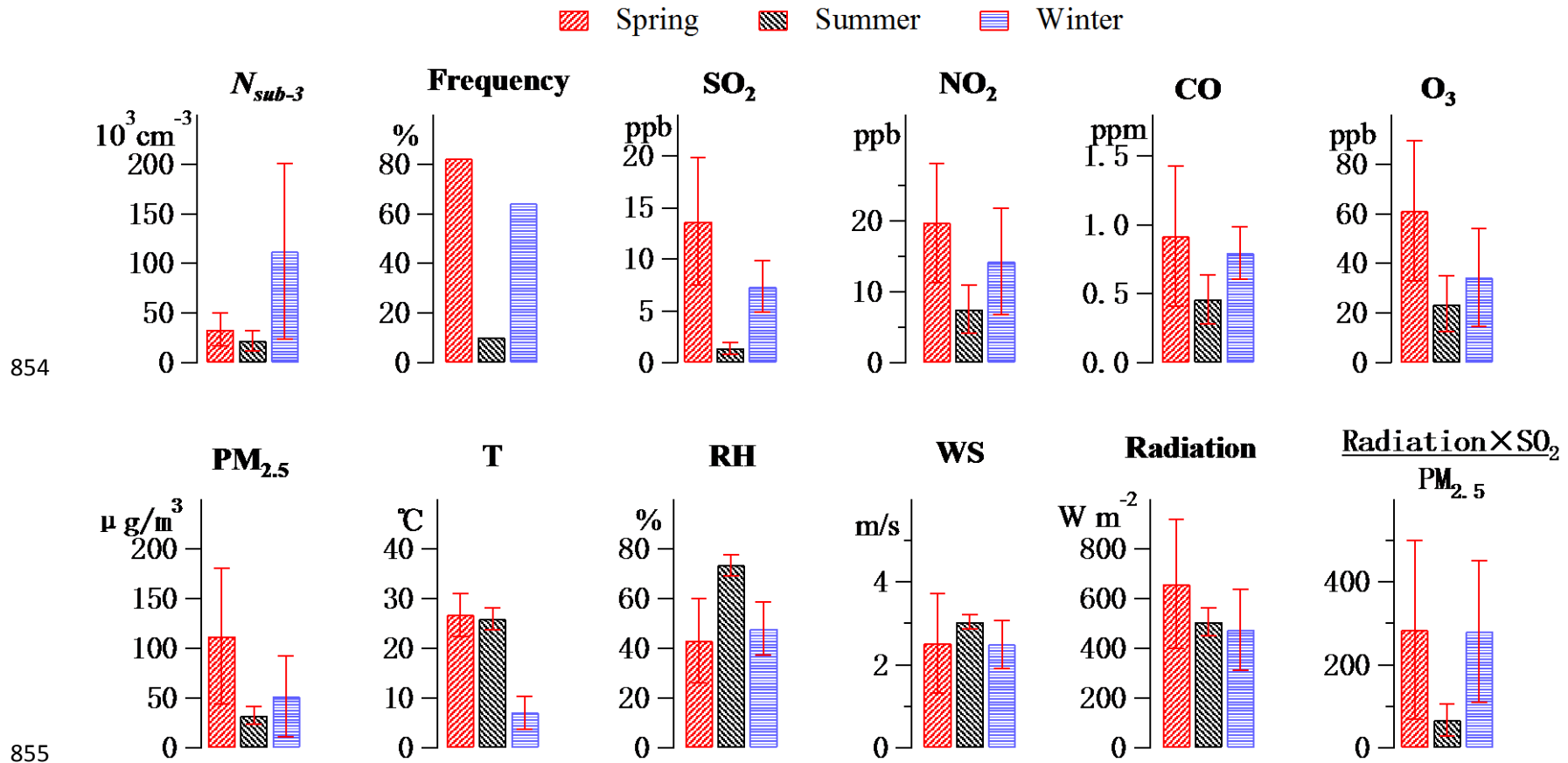
843 Figure 2. N_{sub-3} vs. $J_{1.4}$ in the 8 nucleation events in February, May, December and August during
844 2014-2015. The events were indicated by different colors (blue: March 1, 2015; green: February
845 18, 2015; red: February 19, 2015; purple: August 15, 2014; black: December 27, 2014; grey:
846 May 15, 2014; orange: May 20, 2014; yellow: May 16, 2014)

847

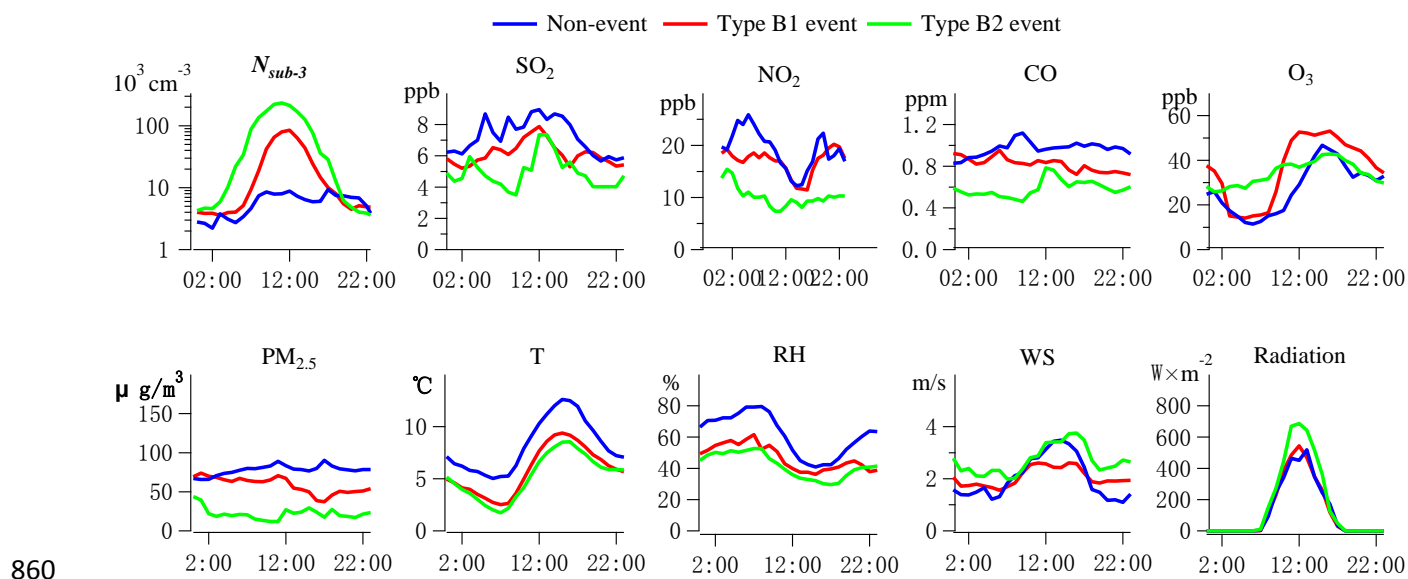


849

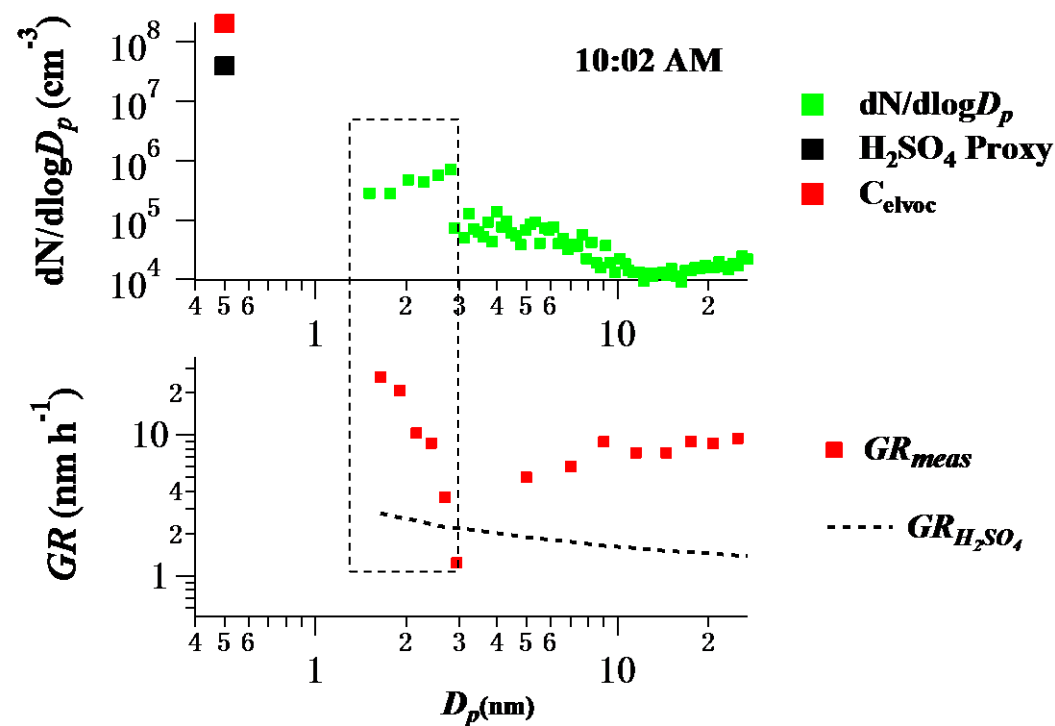
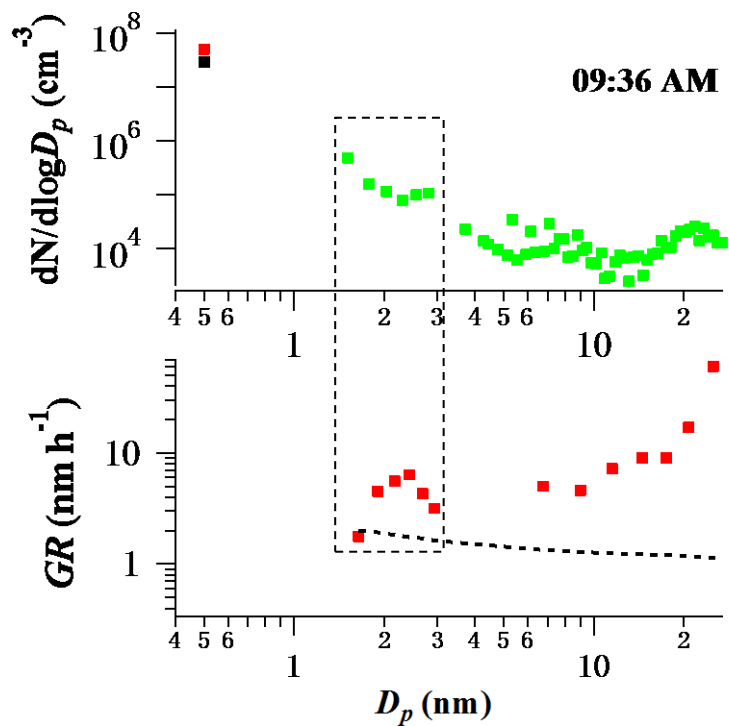
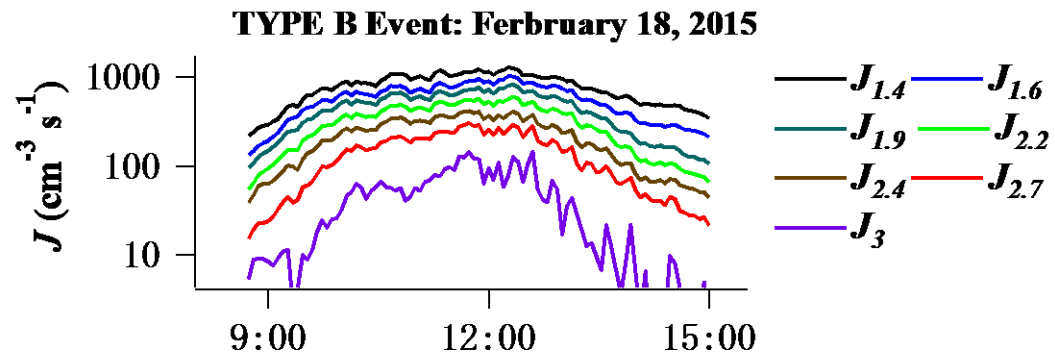
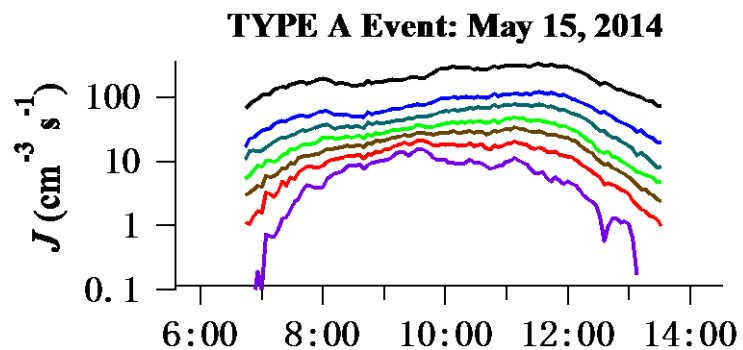
850 Figure 3. Size spectra of typical (a) Type A1 event on May 15, 2014; (b) Type A2 event on May 20,
 851 2014; (3) Type B1 event on February 18, 2015 and (d) Type B2 event on February 19, 2015 during
 852 our measurement period. Size spectra from 3-300 nm (logarithmic scale) and 1.4-3 nm (linear scale)
 853 were obtained using SMPS and nCNC, respectively.



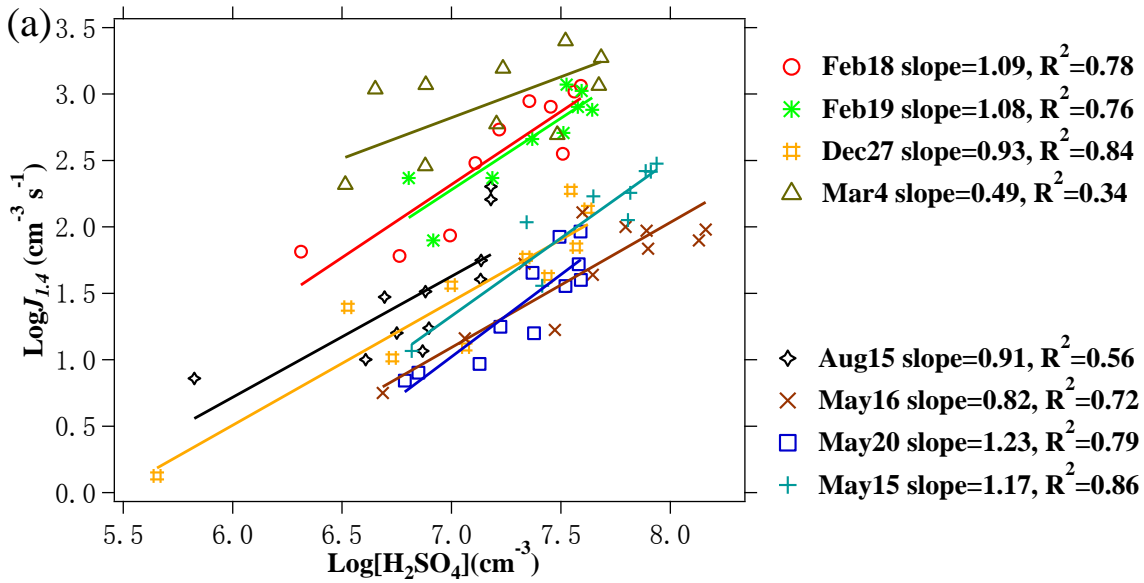
856 Figure 4. Mean and standard deviation of event-averaged N_{sub-3} , anthropogenic trace gases (SO_2 , NO_2 , CO and O_3), $\text{PM}_{2.5}$, and meteorological
 857 variables (temperature, RH, wind speed (WS), solar radiation, and radiation $\times \text{SO}_2 / \text{PM}_{2.5}$) for nucleation events in spring (n=17), summer (n=3)
 858 and winter (n=14). Nucleation frequency (the percentage of event days out of total measurement days) was also shown.



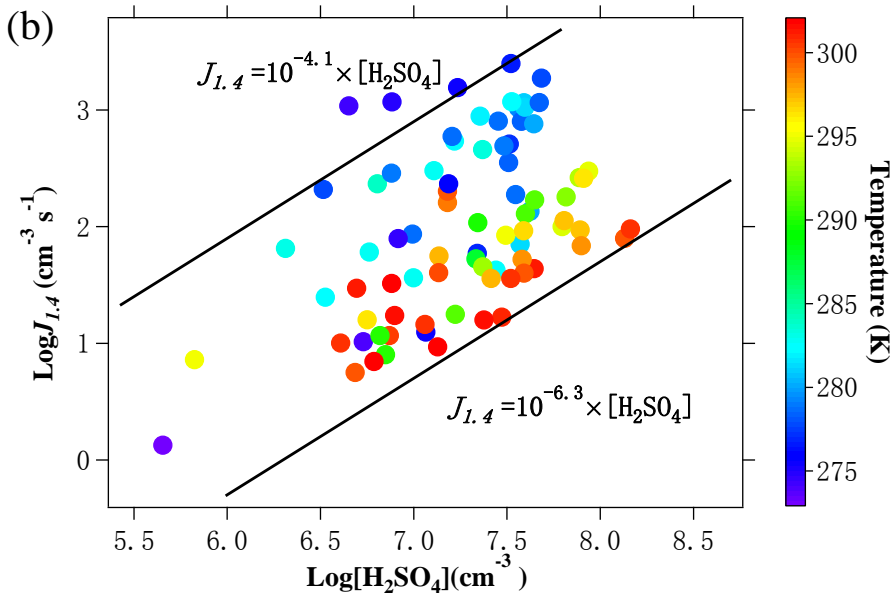
861 Figure 5. Diurnal variations of mean N_{sub-3} , anthropogenic trace gases (SO_2 , NO_2 , CO and O_3), $PM_{2.5}$,
 862 and meteorological variables (temperature, RH, wind speed, and solar radiation flux) on non-event
 863 days (n=8, blue line) and event days (n=3 for Type B1 event, red line and n=6 for Type B2 event,
 864 green line) during winter measurement period.



866 Figure 6. Upper: formation rates (or equivalently, particle growth fluxes) of 1.4, 1.6, 1.9, 2.2, 2.4, 2.7 and 3.0 nm cluster/particles on May 15
867 2014 (Type A1 event) and Feb 18 2015 (Type B1 event). Middle: particle size distribution ($dN/d\log D_p$, green square) selected during the two
868 events (9:36 AM and 10:02 AM). Lower: particle growth rates measured during the same time periods (GR_{meas} , red square). Also shown in the
869 figure were H_2SO_4 proxy (black square) and growth rates calculated from the H_2SO_4 proxy ($GR_{H_2SO_4}$, dashed black line), as well as the
870 calculated ELVOC concentration (C_{elvoc} , red square, see Eq.5) during the same time periods. Dashed boxes in the lower panels highlighted the
871 size distributions and growth rates between 1.4 and 3 nm measured with nCNC.

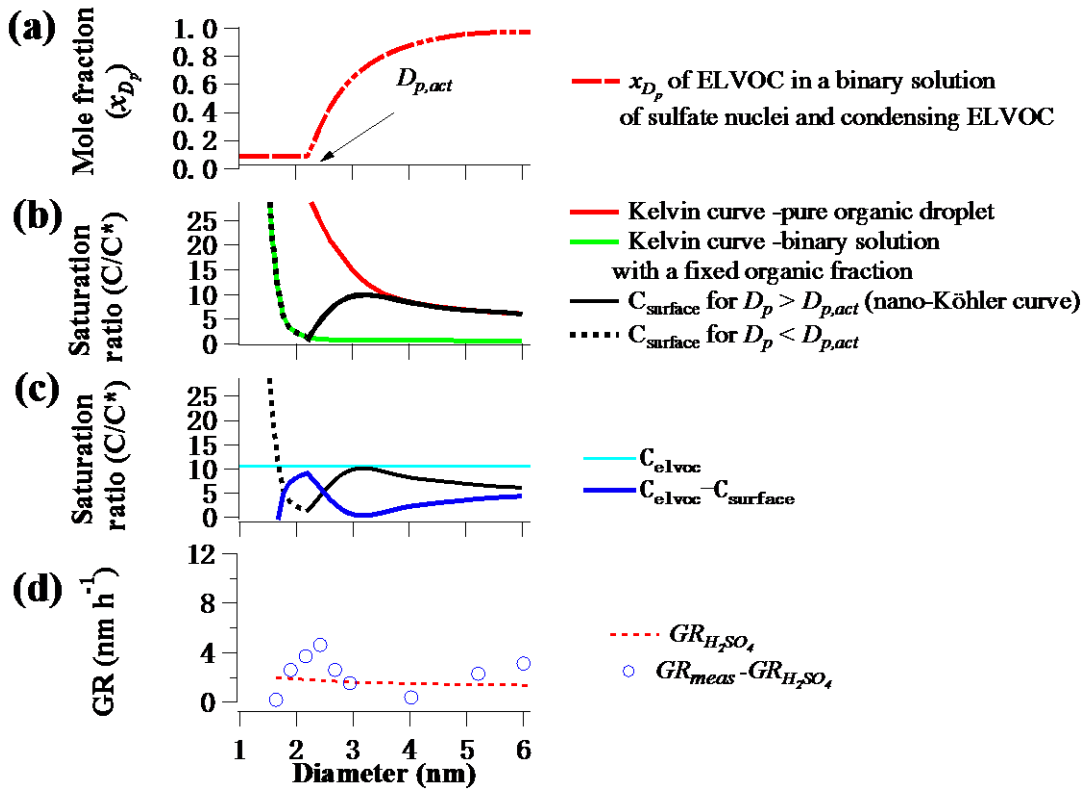


872



873

874 Figure 7. (a) Correlations between $\log J_{1.4}$ and $\log [H_2SO_4]$ for the 8 events. H_2SO_4 proxy was
 875 calculated according to Mikkonen et al. (2011). $J_{1.4}$ and $[H_2SO_4]$ were synchronized to 1 hour that
 876 was the time resolution of solar radiation data. The colored lines showed linear fits to the data of
 877 every single event. (b) The same dataset as (a), but with symbol color to indicate ambient
 878 temperature. Two black lines showed the linear dependences of $J_{1.4}=10^{-4.1} \times [H_2SO_4]$ and $J_{1.4}=10^{-6.3} \times$
 879 $[H_2SO_4]$, between which most of data points located.



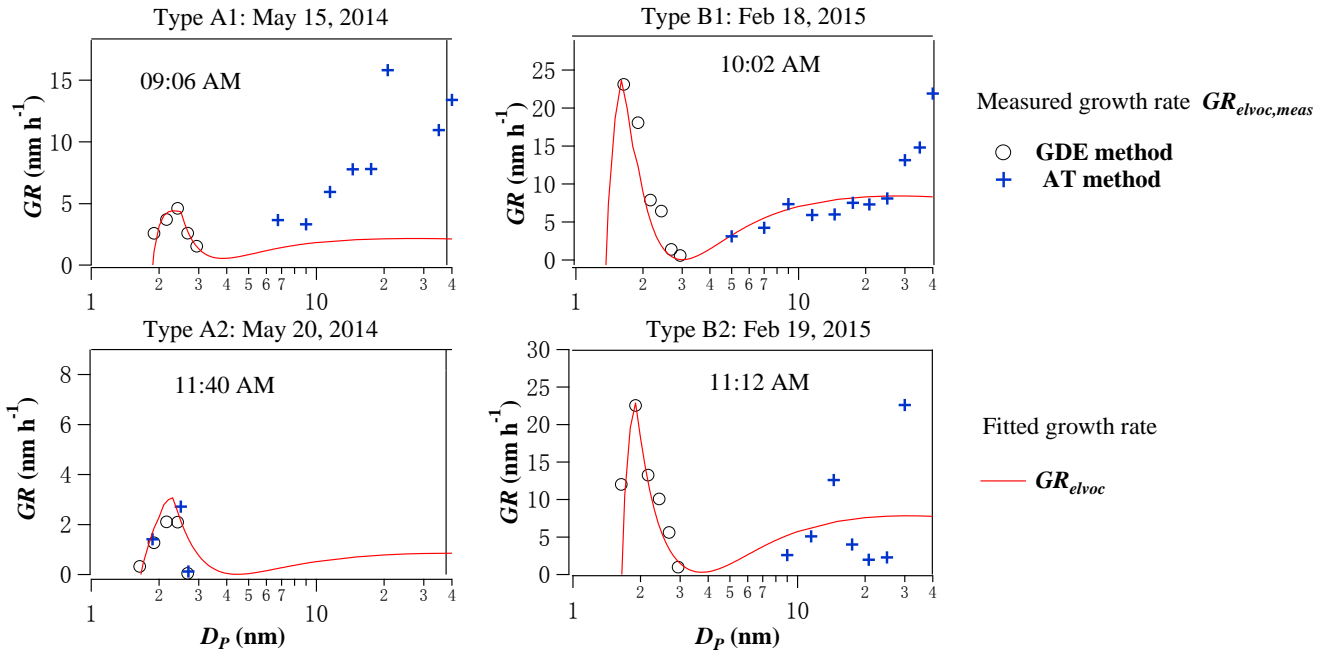
880

881 Figure 8. (a) Mole fraction of organics (x_{D_p}) in a binary solution of sulfate nuclei and activating
 882 organics (ELVOC) in a new particle. Nuclei activation diameter $D_{p,act}$ is the size where ELVOC
 883 begins to dilute the nuclei. (b) Kelvin equilibrium curves over a pure organic droplet (red line) and a
 884 binary solution with a fixed organic fraction (green line), nano Köhler curve for $D_p > D_{p,act}$ (black
 885 solid line) and surface concentration $C_{surface}$ for $D_p < D_{p,act}$ (black dashed line). (c) gas phase
 886 concentration of the organic vapor (C_{elvoc} , cyan line), surface concentration C_{∞} (black line), and
 887 $C_{elvoc} - C_{surface}$ (blue line). (d) Growth rate $GR_{H_2SO_4}$ due to H_2SO_4 (Mikkonen et al. 2011 proxy)
 888 and growth rate due to organic vapor $GR_{elvoc,meas}$, calculated as $GR_{meas} - GR_{H_2SO_4}$.

889

890

891



892

893

894 Figure 9. Comparisons of measured ($GR_{elvoc,meas}$, black circle) and fitted (GR_{elvoc} , red line) growth

895 rates from Eq. (4) for typical Type A1, A2, B1, and B2 events. Also shown were growth rates

896 calculated from appearance time method (blue cross) for sub-3 nm particles when growth rate was

897 relatively small or for larger particles with large size intervals.

898